# Supplementary Information

**Spin-conserved oxygen-redox coupling enables durable anion exchange membrane water electrolysis**

**Authors**

Haochen Li[1#], Haoyin Zhong[1#*], Qi Zhang[1], Wen Cui[1], Wanting Zhang[1], Youyu Tian[1], Guangxin Sun[2], Tieyang Zhao[1], Caozheng Diao[3], Zhi Gen Yu[4], Baorui Jia[1,5], Shibo Xi[1,6], Junmin Xue[1*]

**Affiliations**

[1] Department of Materials Science and Engineering, National University of Singapore, Singapore, 117575, Singapore.

[2] Suzhou Nuclear Power Research Institute Co., Ltd., Suzhou, 215004, China.

[3] Singapore Synchrotron Light Sources (SSLS), National University of Singapore, 117603, Singapore

[4] Institute of Advanced Intelligence and Computing (IAIC), Agency for Science, Technology and Research, Singapore, 138632, Singapore

[5] Institute for Advanced Materials and Technology, University of Science and Technology Beijing, Beijing 10083, China.

[6] Institute of Sustainability for Chemical, Energy and Environment (ISCE[2]), Agency for Science, Technology and Research, Singapore, 627833, Singapore.

[#]Equal contribution

[*]Correspondence to: msexuejm@nus.edu.sg (Junmin Xue); stbzzhy@nus.edu.sg (Haoyin Zhong)

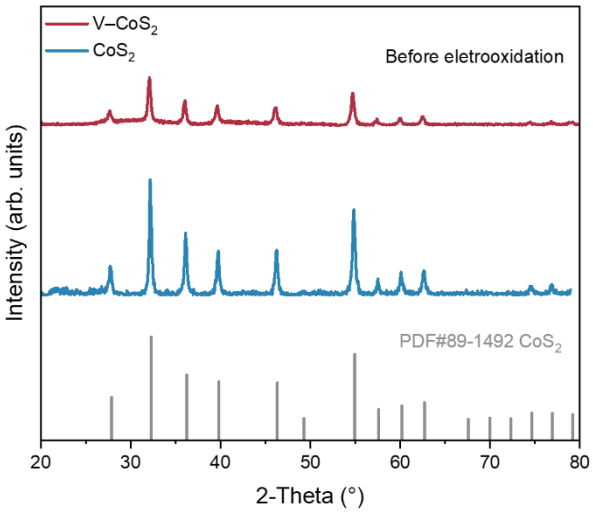


**Supplementary Fig.1 |** XRD patterns of V−incorporated $CoS_2$ samples and $CoS_2$.

The X-ray diffraction (XRD) pattern of the as-prepared sample agrees well with the standard diffraction peaks of $CoS_2$ (PDF#89-1492), indicating the formation of the sulfide phase without detectable crystalline impurities. Upon V incorporation, the $CoS_2$ sample exhibits a systematic shift of the characteristic diffraction peaks toward lower 2θ values relative to the undoped counterpart. This peak displacement suggests an expansion of the lattice parameter, consistent with the incorporation of V species into the $CoS_2$ framework rather than the formation of a separate crystalline V-containing phase. No additional impurity reflections are observed within the detection limit of the measurement.

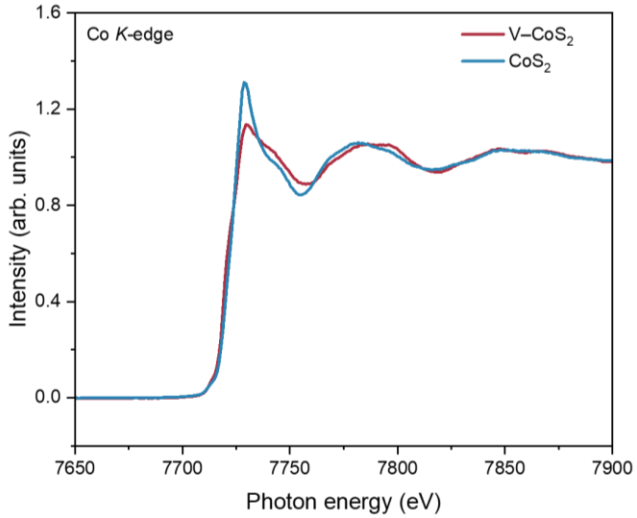


**Supplementary Fig.2 |** Co *K*-edge X-ray absorption spectra of V–$CoS_2$ and $CoS_2$.

Compared with pristine $CoS_2$, the absorption edge of V–$CoS_2$ shifts slightly toward lower photon energy, indicating a reduced average oxidation state of Co after V incorporation. This behavior suggests that the introduction of high-valence V species induces electronic redistribution within the $CoS_2$ lattice, leading to partial electron enrichment at neighboring Co centers.

Such an electronic effect is consistent with the presence of high-valence V dopants in the precursor, as independently supported by the V 2*p* XPS results, which identify the incorporated vanadium species as predominantly $V^{5+}$. Therefore, although V is introduced as a high-valence dopant, its incorporation leads to a lowered average Co valence through local charge compensation and electronic structure reorganization within the $CoS_2$ framework.

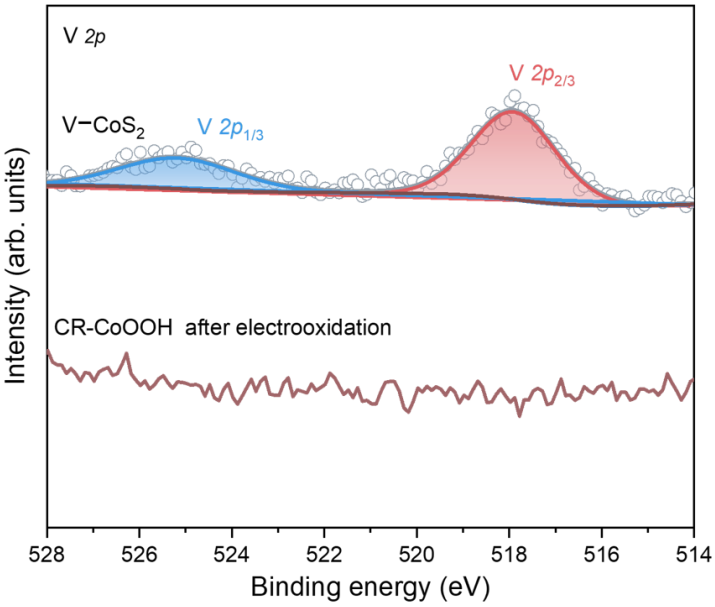


**Supplementary Fig.3 | XPS characterization of V–$CoS_2$ before and after electrochemical oxidation.** Top: V 2*p* spectrum of V–$CoS_2$ showing characteristic V $2p_{2/3}$ and V $2p_{1/2}$ peaks. Bottom: V 2*p* spectrum of CR-CoOOH after electrochemical oxidation, where no detectable V signal is observed.

The V 2*p* XPS spectrum of V–$CoS_2$ shows two characteristic peaks located at 517.9 and 525.1 eV, which are assigned to V $2p_{3/2}$ and V $2p_{1/2}$, respectively. The binding energies are consistent with V in a high oxidation state ($V^{5+}$). This result is also consistent with the XRD observations, where V incorporation induces a shift of the $CoS_2$ diffraction peaks toward lower 2θ values. Although $V^{5+}$ has a smaller ionic radius than Co, the observed lattice expansion is more plausibly attributed to charge redistribution and local structural distortion induced by the high-valence dopant, rather than to a simple ionic size effect.

After electrochemical activation, no detectable V 2*p* signal is observed in the XPS spectrum of CR-CoOOH within the detection limit of the measurement. This result indicates that V species are substantially depleted from the surface region probed by XPS, suggesting extensive dissolution of V during electrochemical reconstruction.

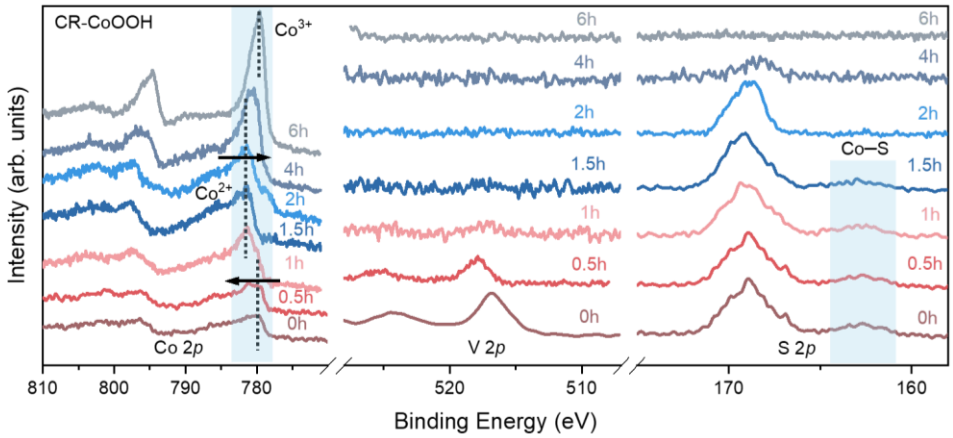


**Supplementary Fig.4 |** High-resolution Co 2*p*, V 2*p*, and S 2*p* XPS spectra of CR-CoOOH recorded after different electrochemical activation times (0-6 h).

Time-dependent XPS measurements were performed to monitor the compositional evolution of CR-CoOOH during electrochemical activation. As the activation time increases from 0 to 6 h, a progressive attenuation of the V 2*p* signal is observed, with the V signal becoming nearly undetectable at extended activation times. In contrast, the S 2*p* signal remains discernible at intermediate stages before gradually diminishing.

The more rapid decrease of the V 2*p* intensity relative to the S 2*p* signal indicates that V species are preferentially depleted from the near-surface region during electrochemical activation. This behavior suggests that high-valence V species are more susceptible to electrochemical leaching compared to sulfur species within the sulfide framework.

Simultaneously, the Co 2*p* spectra exhibit a gradual evolution with increasing activation time. At the initial stage (0 h), the spectrum contains noticeable contributions from $Co^{2+}$ species, characteristic of the sulfide precursor. As electrochemical activation proceeds, the relative intensity of the $Co^{3+}$ component progressively increases, accompanied by a reduction in the $Co^{2+}$ contribution and changes in the satellite features. After prolonged activation, the spectra are dominated by $Co^{3+}$-related peaks, indicative of the formation of cobalt oxyhydroxide species.

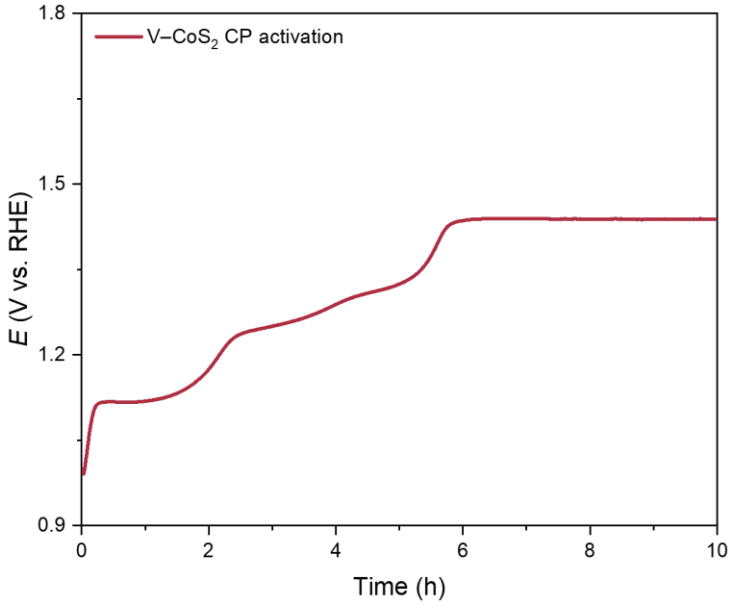


**Supplementary Fig.5 |** Chronopotentiometric reconstruction profile of V–$CoS_2$ at 10 mA $cm^{-2}$.

The potential evolves during oxidative reconstruction and reaches a stable plateau after approximately 10 h, indicating that the reconstructed CR-CoOOH active phase has reached a stable catalytic state.

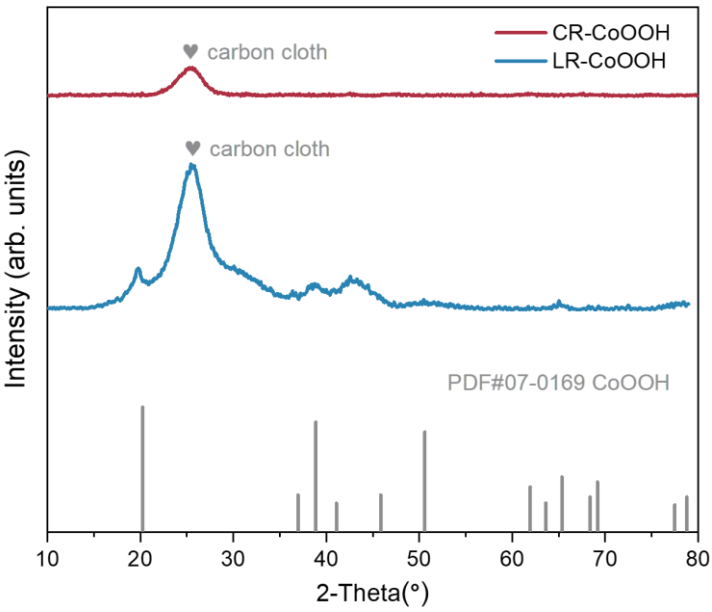


**Supplementary Fig.6** | XRD pattern of the reconstructed sample CR-CoOOH and LR-CoOOH after electrochemical operation

After electrochemical reconstruction, the XRD pattern of CR-CoOOH shows no clearly resolved diffraction peaks assignable to crystalline cobalt oxyhydroxide. Instead, the diffraction profile is dominated by broad and diffuse features, indicating the absence of detectable long-range crystallographic order within the resolution of XRD. In contrast, the LR-CoOOH sample displays discernible diffraction peaks after electrochemical oxidation, which can be indexed to the CoOOH phase, reflecting the formation of a more ordered oxyhydroxide structure.

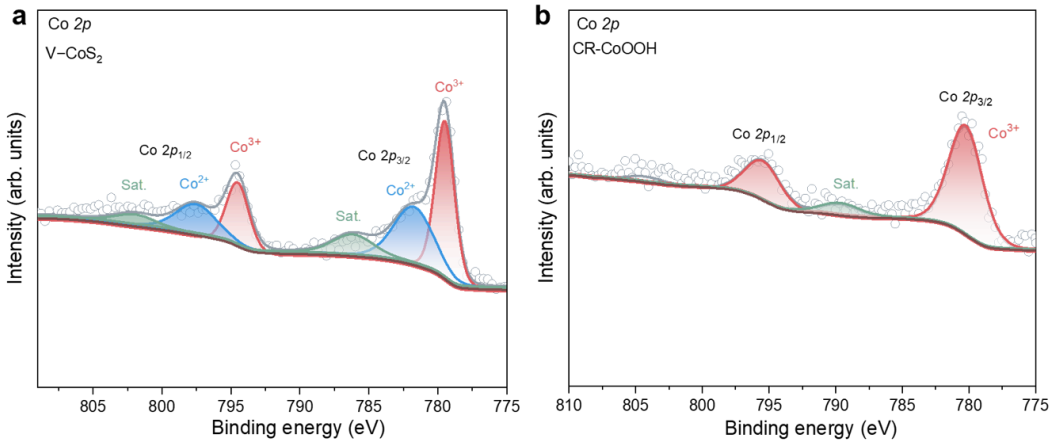


**Supplementary Fig.7 | High-resolution Co 2*p* XPS spectra. a** Co 2*p* XPS spectra of and V–$CoS_2$. **b** Co 2*p* XPS spectra of CR-CoOOH after electrochemical reconstruction.

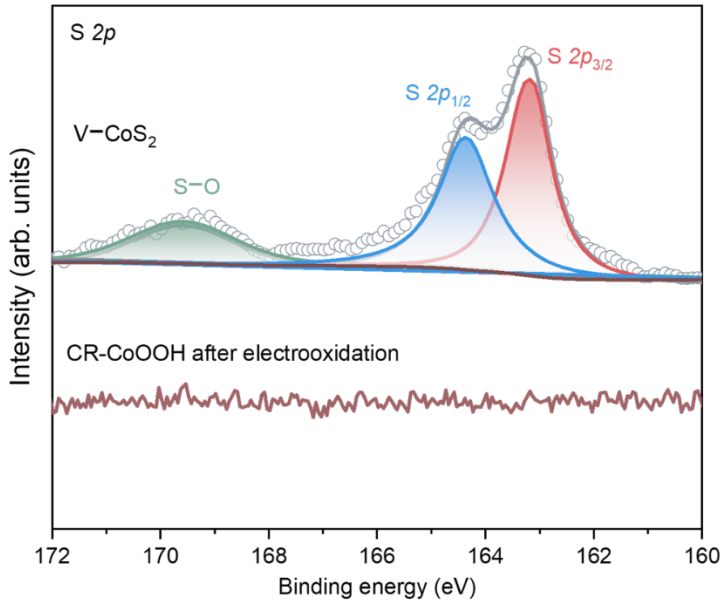


**Supplementary Fig.8 |** High-resolution S 2*p* XPS spectra of pristine V−$CoS_2$ and CR-CoOOH.

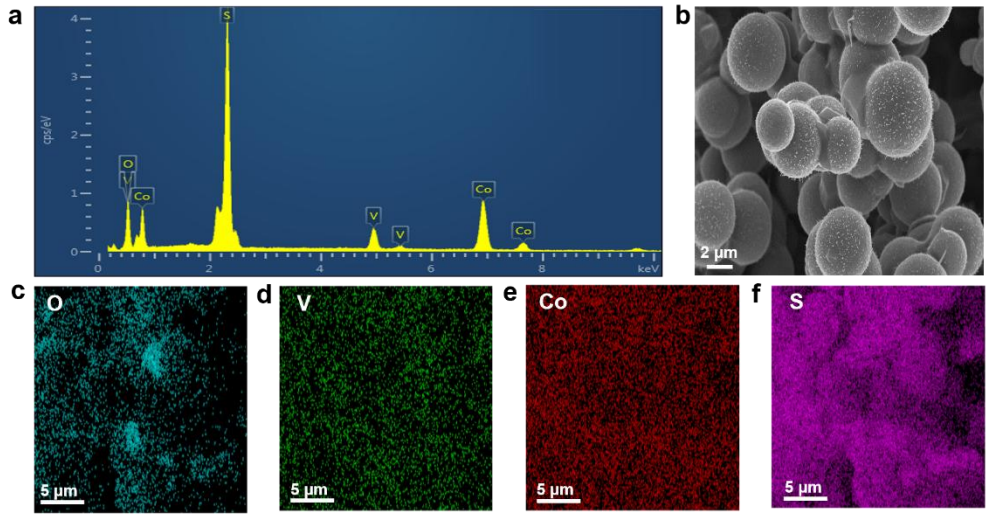


**Supplementary Fig. 9 | Morphology and elemental distribution of the V−$CoS_2$ precursor.** a, EDS spectrum of the V−$CoS_2$ precursor showing the characteristic signals of V, Co, S and O. **b**, SEM image showing the spherical morphology and textured surfaces of the precursor particles. **c**, EDS elemental map of O. **d**, EDS elemental map of V. **e**, EDS elemental map of Co. **f**, EDS elemental map of S. The spatially homogeneous distribution of V alongside Co and S confirms the successful incorporation of V throughout the $CoS_2$ precursor.

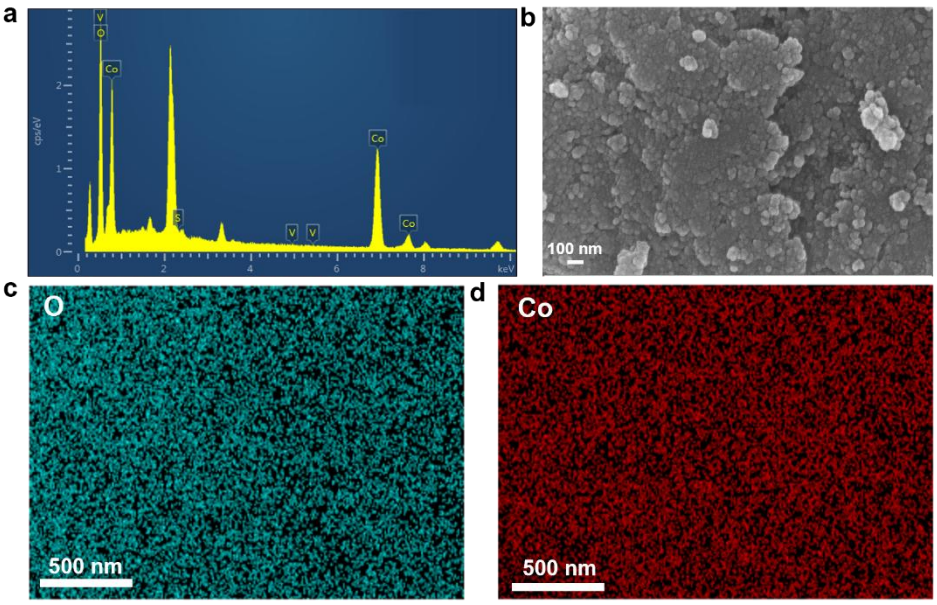


**Supplementary Fig.10 | Morphology and elemental analysis of CR-CoOOH after electrochemical oxidation. a**, EDS spectrum showing predominant Co and O signals after electrochemical oxidation, with V and S below detectable levels. **b**, SEM image of CR-CoOOH after electrochemical reconstruction. **c-d**, Elemental mapping of O (c) and Co (d), indicating a uniform distribution of Co and O throughout the reconstructed structure.

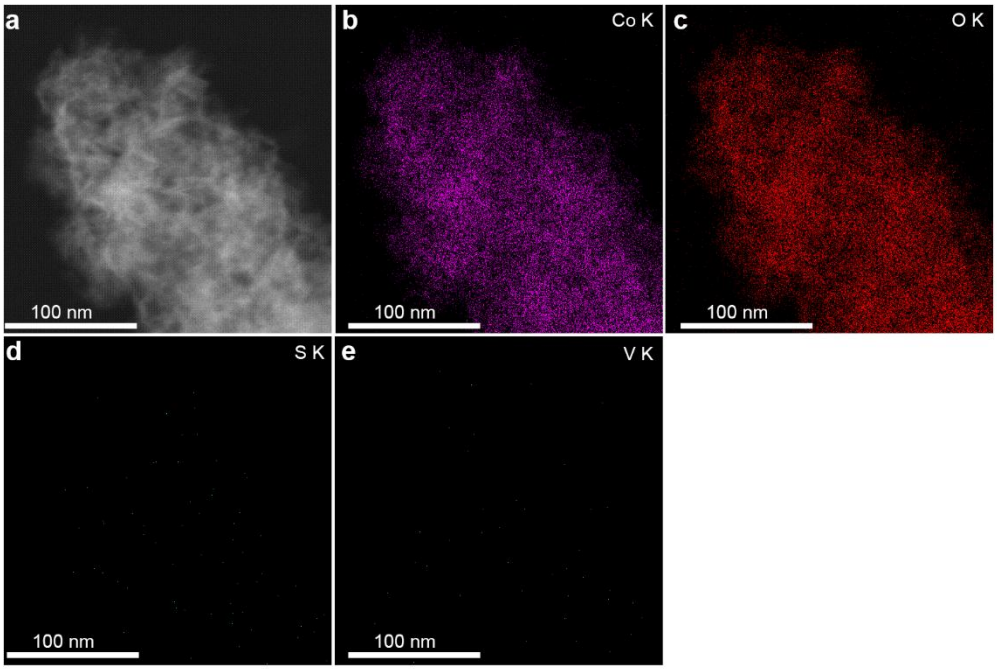


**Supplementary Fig.11 | STEM-EDS elemental mapping of CR-CoOOH.** (a) HAADF-STEM image of CR-CoOOH and the corresponding EDS elemental maps of (b) Co, (c) O, (d) S, and (e) V.

Co and O signals are distributed throughout the observed particle region, confirming the CoOOH-based reconstructed structure. In contrast, negligible S and V signals are observed, suggesting the complete removal of sulfur- and vanadium-related species after reconstruction.

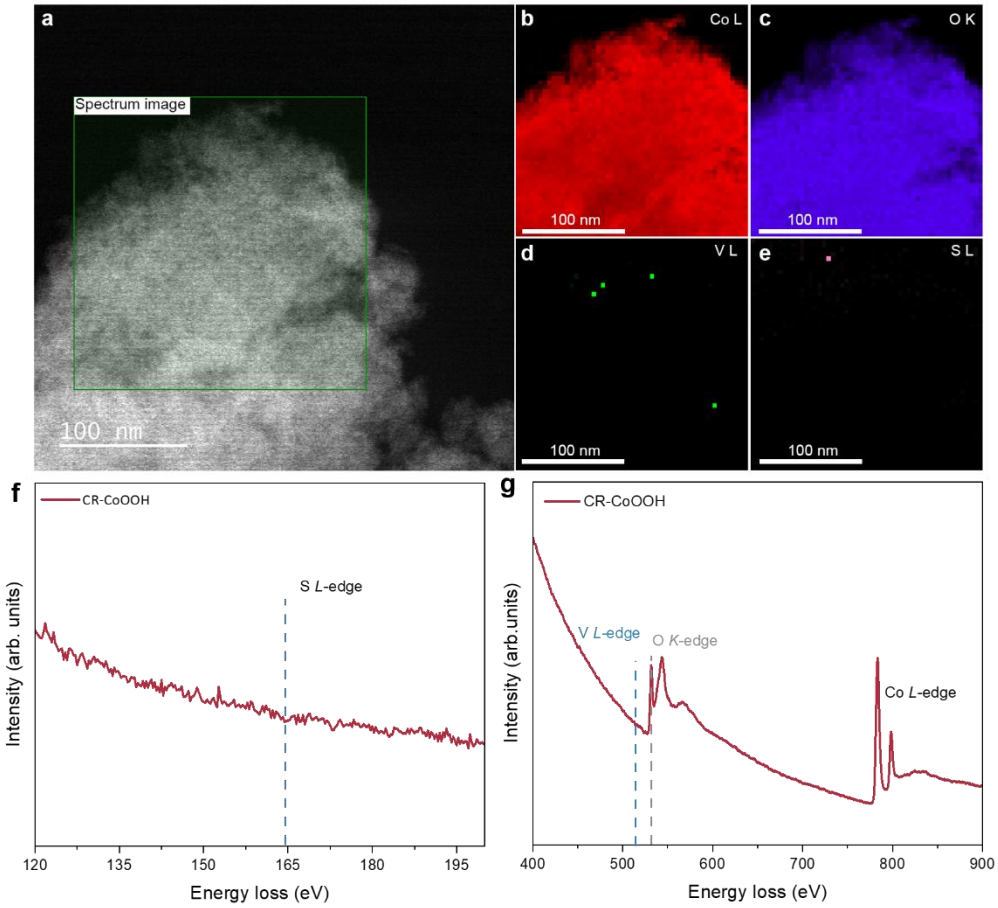


**Supplementary Fig. 12 | STEM-EELS characterization of CR-CoOOH. a**, HAADF-STEM image of CR-CoOOH with the selected spectrum-imaging region marked by the green box. **b**, EELS elemental map of the Co *L*-edge. **c**, EELS elemental map of the O *K*-edge. **d**, EELS elemental map of the V *L*-edge. **e**, EELS elemental map of the S *L*-edge. **f**, Representative EELS spectrum in the S *L*-edge energy region, showing no discernible S signal. **g**, Representative EELS spectrum covering the V *L*- and O *K*-edge regions. The absence of a discernible V *L*-edge signal and the pronounced O *K*-edge feature indicate the nearly complete removal of residual V from CR-CoOOH. The expected edge-onset positions are marked by dashed lines.

The Co and O signals are clearly distributed across the reconstructed CoOOH region, whereas negligible V and S signals are observed. The bottom panels show representative EELS spectra collected from the mapped region, further confirming the dominant Co–O framework and the complete removal of V/S species after reconstruction.

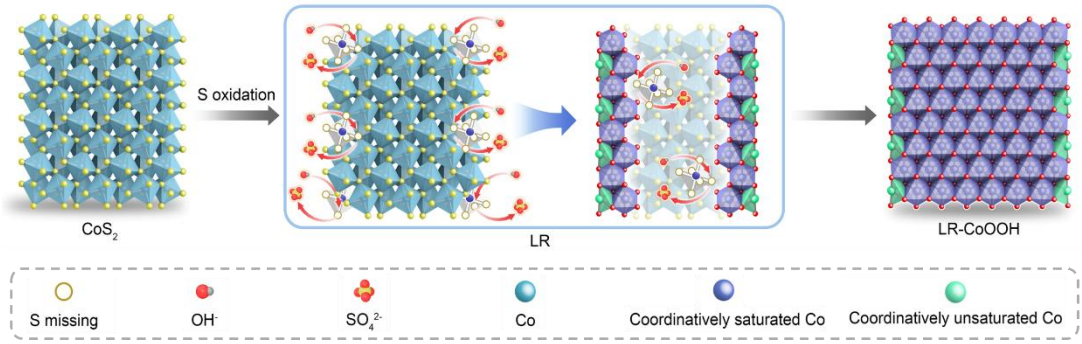


**Supplementary Fig.13 |** Schematic illustration of localized reconstruction (LR). Edge-initiated localized reconstruction of $CoS_2$ leading to LR-CoOOH.

For the V-free $CoS_2$ precursor, electrochemical oxidation primarily initiates at edge sites, where sulfur oxidation occurs preferentially. The reconstruction then gradually propagates inward from these edge regions, forming a reconstructed oxyhydroxide phase (LR-CoOOH). In this edge-initiated reconstruction pathway, coordinatively unsaturated Co sites are mainly generated near edge regions. In contrast, when V is incorporated into the $CoS_2$ lattice, electrochemical activation induces the preferential oxidation and dissolution of V species. The removal of V creates local lattice vacancies and destabilizes the surrounding sulfur environment. As a result, sulfur atoms adjacent to the dissolved V sites undergo oxidation, triggering structural reconstruction within the lattice interior rather than only at edges. These internally initiated reconstruction events propagate outward and lead to a cascade reconstruction process.

Consequently, unlike the edge-limited reconstruction observed in LR, the cascade reconstruction produces coordinatively unsaturated Co centers throughout the lattice. The resulting CR-CoOOH therefore contains a higher density of unsaturated Co sites and neighboring active centers compared with LR-CoOOH.

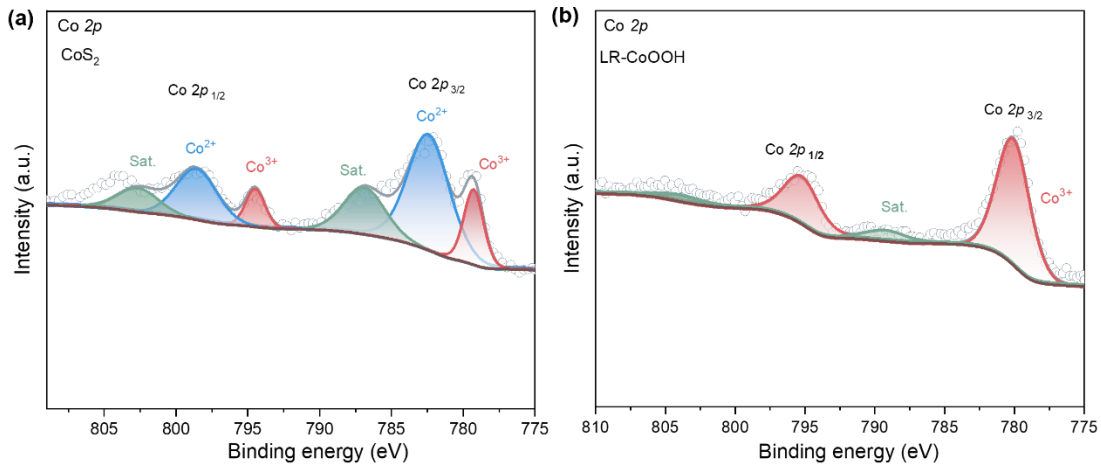


**Supplementary Fig.14 | High-resolution Co 2*p* XPS spectra. a**, Co 2*p* XPS spectra of pristine $CoS_2$. **b**, Co 2*p* XPS spectra of LR-CoOOH after electrochemical reconstruction.

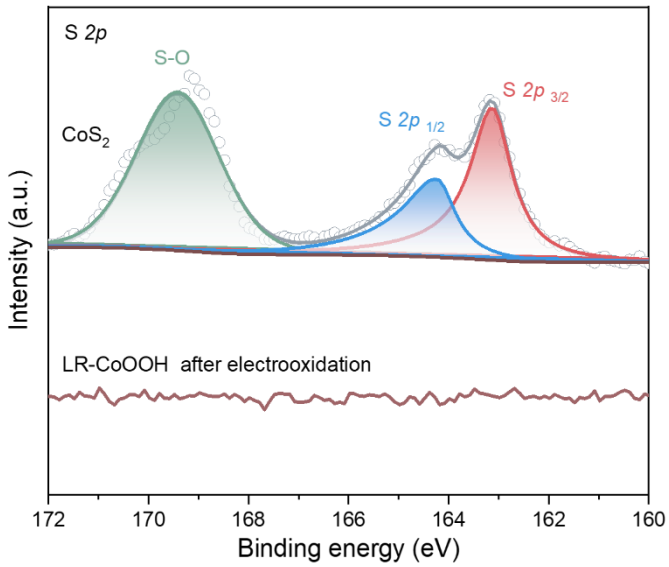


**Supplementary Fig.15** | High-resolution S 2*p* XPS spectra of pristine $CoS_2$ and LR-CoOOH after electrochemical oxidation.

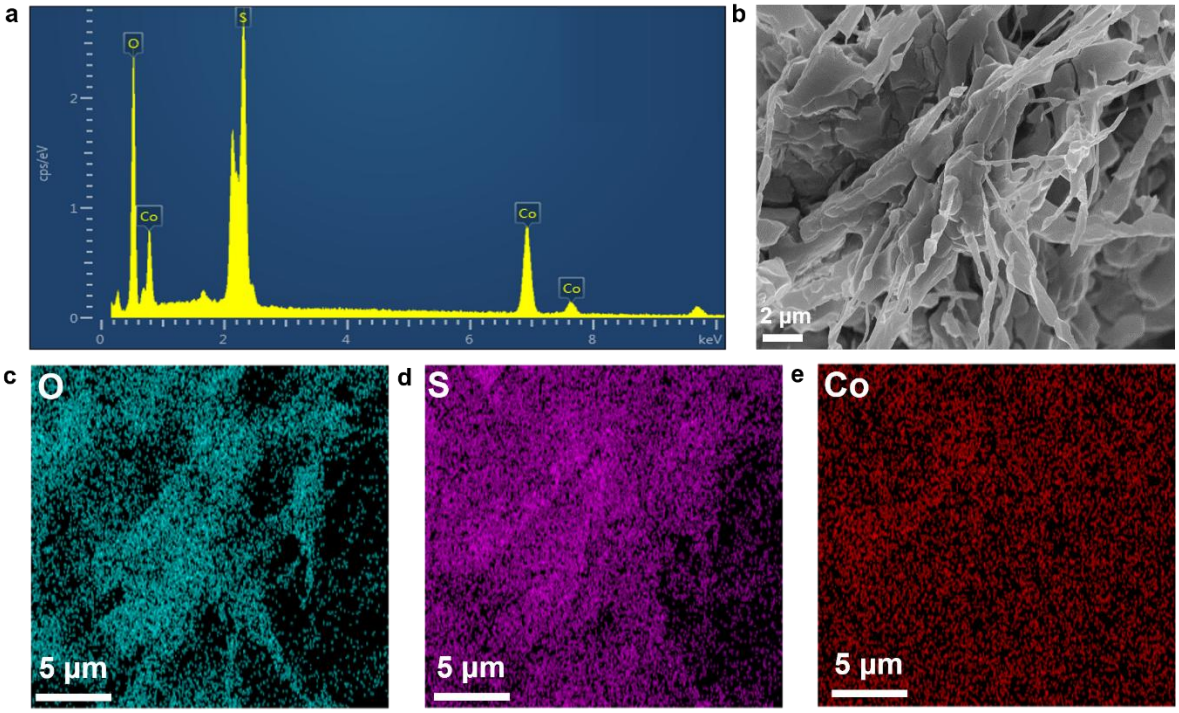


**Supplementary Fig. 16 | Morphology and elemental distribution of the $CoS_2$ precursor. a**, EDS spectrum of the $CoS_2$ precursor showing the characteristic Co and S signals. **b**, SEM image revealing the interconnected layered morphology of the precursor. **c**, EDS elemental map of O. **d**, EDS elemental map of S. **e**, EDS elemental map of Co, demonstrating the spatial distribution of Co throughout the precursor**.**

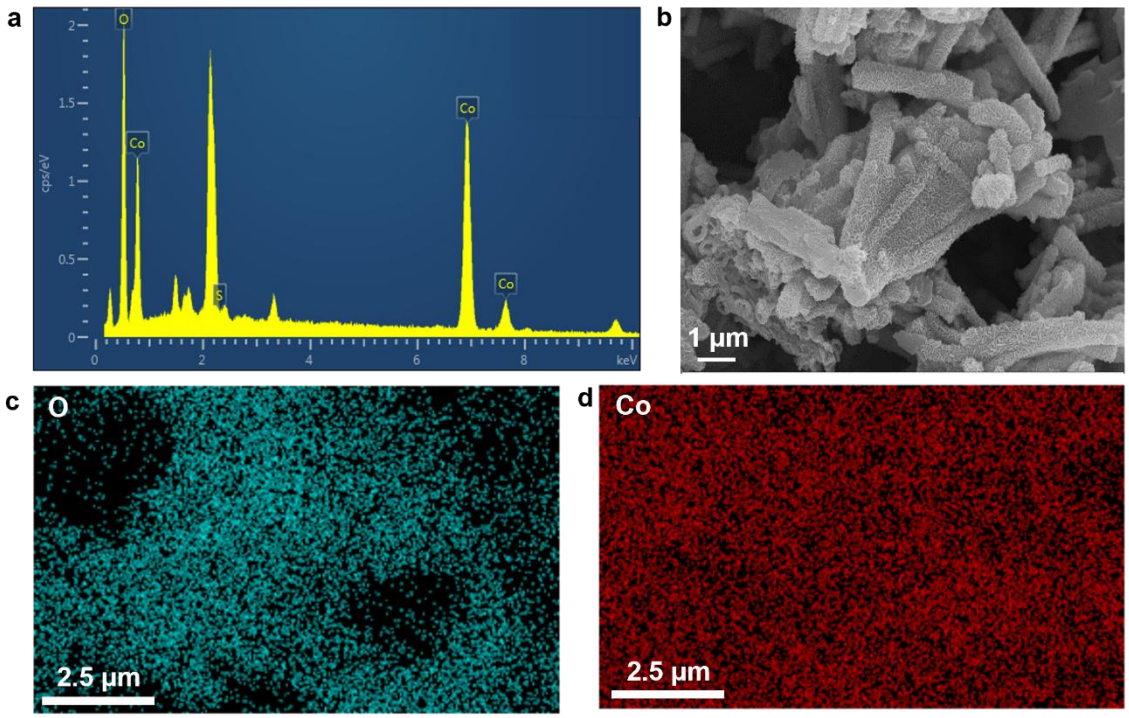


**Supplementary Fig. 17 | Structural characterization of LR-CoOOH after electrochemical oxidation. a,** EDS spectrum of LR-CoOOH showing dominant Co and O signals, with only a barely detectable S signal. **b**, SEM image of the reconstructed catalyst, displaying a rough and porous surface morphology. **c**, EDS elemental map of O. **d**, EDS elemental map of Co, revealing the spatial distribution of Co throughout the reconstructed catalyst**.**

Although V-$CoS_2$ and $CoS_2$ show differences in precursor morphology and surface XPS features, these pristine sulfide precursors are not the final catalytically active phases under OER conditions. Both precursors undergo electrochemical reconstruction into oxyhydroxide active phases before OER evaluation, yielding CR-CoOOH and LR-CoOOH, respectively. Therefore, the performance difference between CR-CoOOH and LR-CoOOH should be evaluated primarily based on the reconstructed oxyhydroxide phases rather than the pristine sulfide precursors.

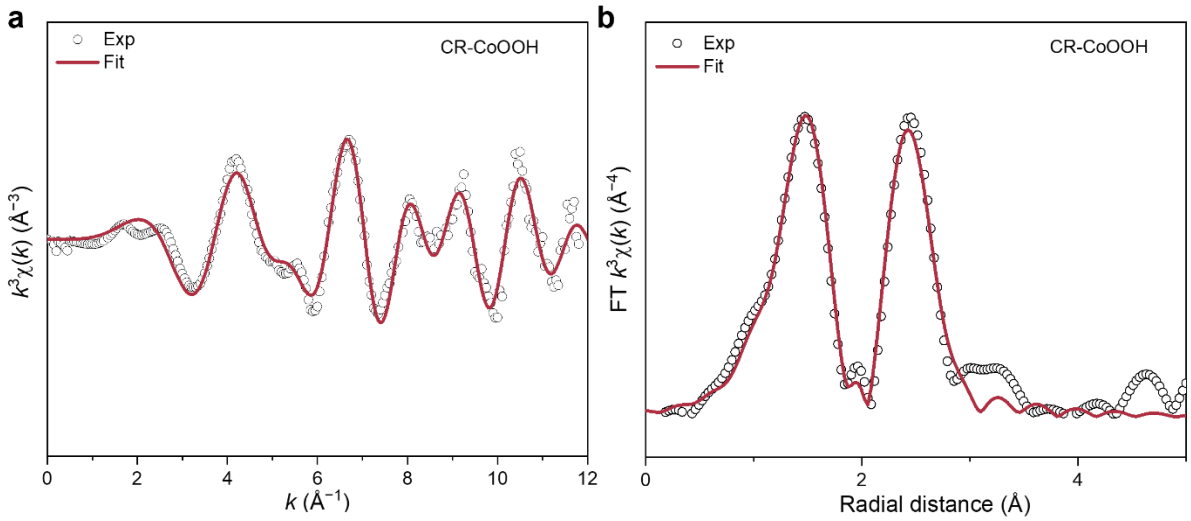


**Supplementary Fig.18 | EXAFS fitting analysis of CR-CoOOH at the Co *K*-edge. a**, Experimental data (symbols) and fitting curves (solid lines) in k space. **b**, Fourier-transformed EXAFS spectra in R space with the corresponding fitting results.

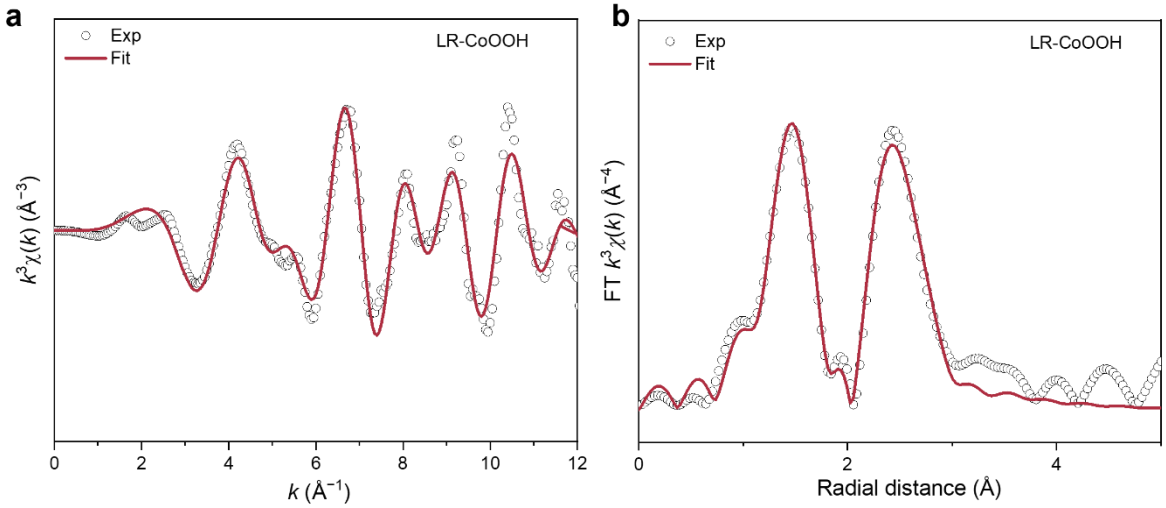


**Supplementary Fig.19 | EXAFS fitting results of LR-CoOOH at the Co *K*-edge. a**, Experimental data (open circles) and fitted curve (solid line) of the EXAFS spectra in k space. **b**, Corresponding Fourier-transformed EXAFS spectra and fitting curves in R space.

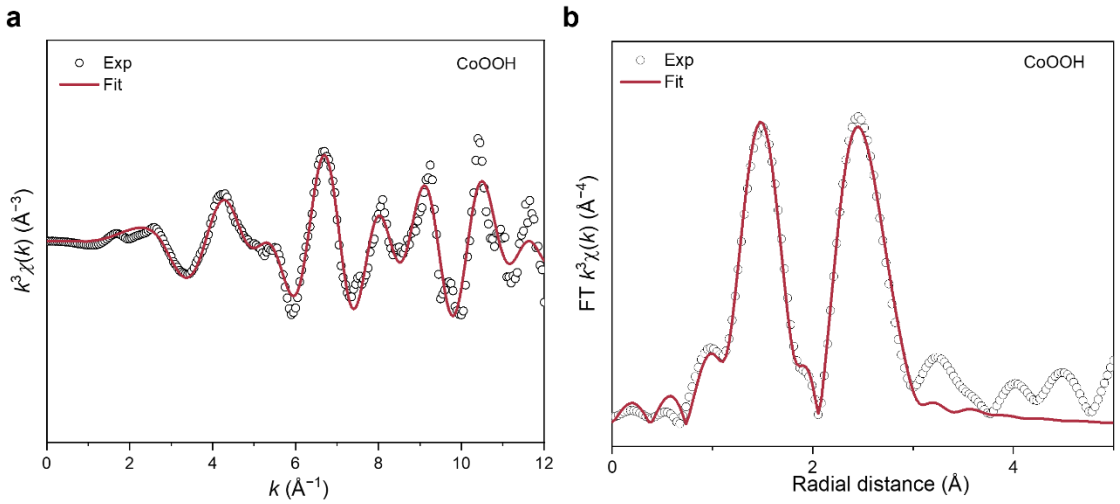


**Supplementary Fig.20 | EXAFS fitting results of CoOOH at the Co *K*-edge. a**, Experimental data (open circles) and fitted curve (solid line) of the EXAFS spectra in k space. **b**, Corresponding Fourier-transformed EXAFS spectra and fitting curves in R space.

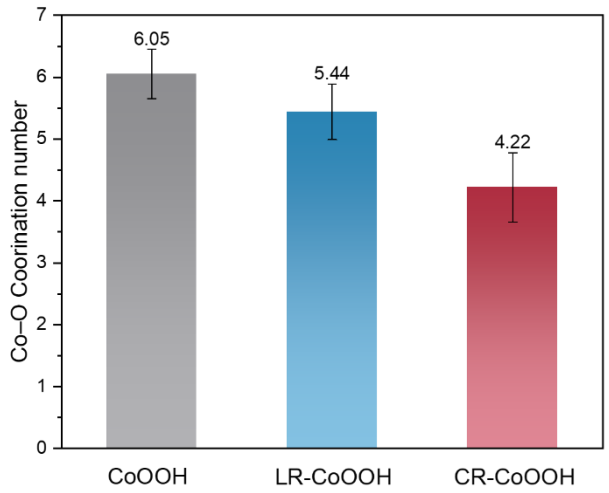


**Supplementary Fig.21 |** Comparison of the Co–O coordination numbers obtained from EXAFS fitting. Error bars represent fitting uncertainties from EXAFS analysis.

To quantitatively analyze the local coordination structure, EXAFS fitting was conducted and the Co–O coordination numbers were extracted. The fitting results show that CR-CoOOH exhibits a lower Co–O coordination number than LR-CoOOH and CoOOH, suggesting the formation of coordinatively unsaturated Co centers after reconstruction. Such a reduction in local coordination is consistent with the structural characteristics expected from the cascade reconstruction process, where the selective dissolution of V and subsequent lattice reorganization generate abundant unsaturated cobalt sites.

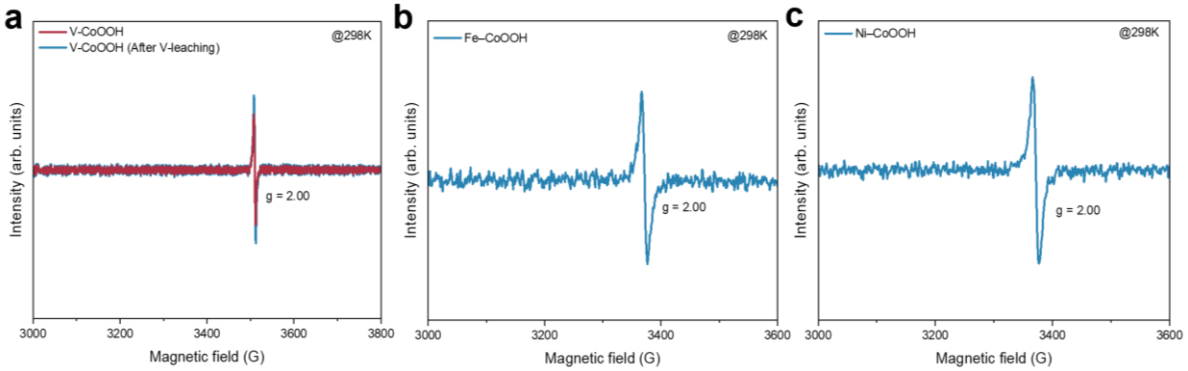


**Supplementary Fig.22 | Control EPR spectra of doped CoOOH samples after electrochemical oxidation. a**, EPR spectrum of directly synthesized V-CoOOH. **b**, EPR spectrum of Fe-CoOOH. **c**, EPR spectrum of Ni-CoOOH. All spectra were recorded at 298 K.

To clarify whether the Co-centered spin signal observed in CR-CoOOH originates simply from heteroatom incorporation, control EPR measurements were performed on directly synthesized V-CoOOH, Fe-doped CoOOH, and Ni-doped CoOOH after electrochemical oxidation. Here, V-CoOOH refers to a vanadium-doped cobalt oxyhydroxide synthesized directly without sulfidation, and was used as a control to distinguish the effect of V incorporation itself from that of the sulfide-derived cascade reconstruction pathway.

In all three control samples, only a resonance centered at $g \approx 2.00$ is observed, which is commonly associated with defect-related paramagnetic centers. No detectable feature attributable to Co-centered unpaired spins appears at $g \approx 2.16$ under the present measurement conditions. These results indicate that heteroatom incorporation alone, even after electrochemical oxidation, is insufficient to generate the Co-centered spin signal observed in CR-CoOOH. Therefore, the emergence of Co-centered unpaired spins in CR-CoOOH should be attributed to the cascade reconstruction process triggered by selective V dissolution in the sulfide-derived precursor, rather than to dopant incorporation itself.

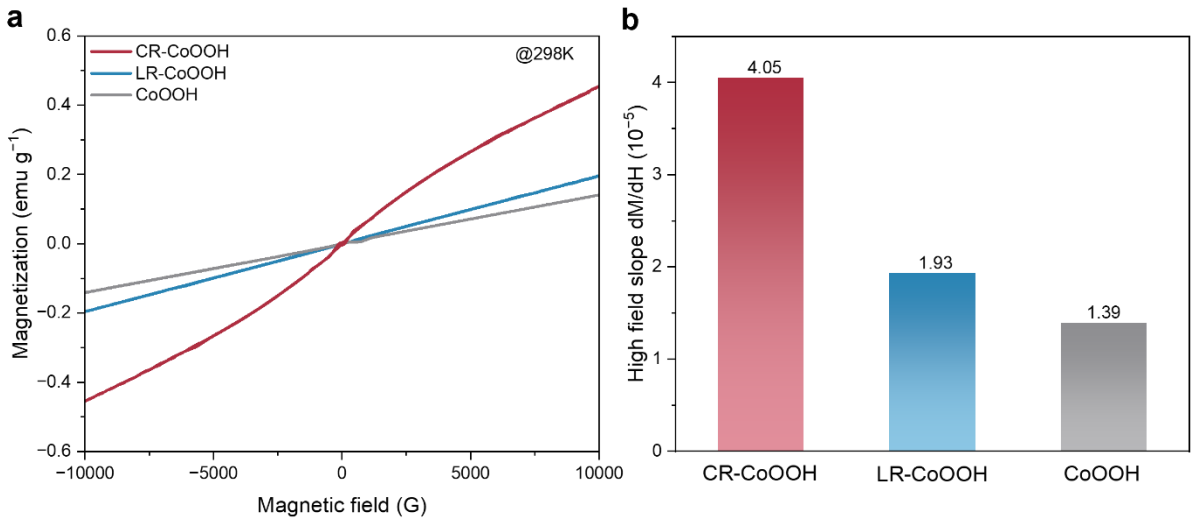


**Supplementary Fig.23 | Room-temperature magnetic measurements of reconstructed catalysts. a**, M–H curves of CR-CoOOH, LR-CoOOH, and CoOOH recorded at room temperature. **b**, High-field slopes (dM/dH) derived from the corresponding M–H curves, reflecting the relative magnetic susceptibilities of the samples

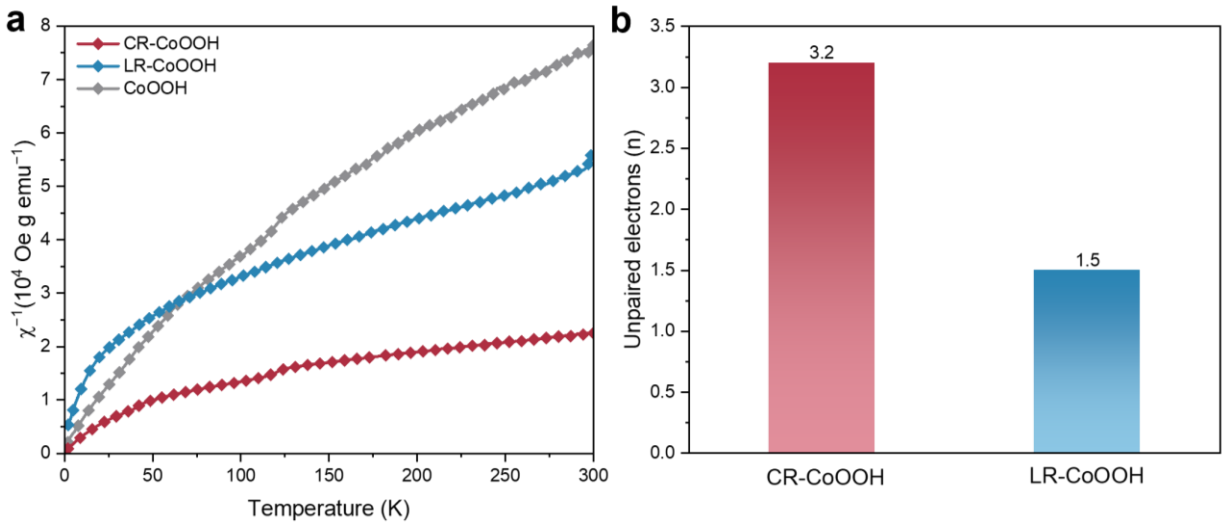


**Supplementary Fig.24 | Temperature-dependent magnetization analysis**. **a**, Magnetization–temperature (M–T) curves of CR-CoOOH, LR-CoOOH, and CoOOH. **b**, Number of unpaired electrons derived from Curie-law fitting of the M–T curves.

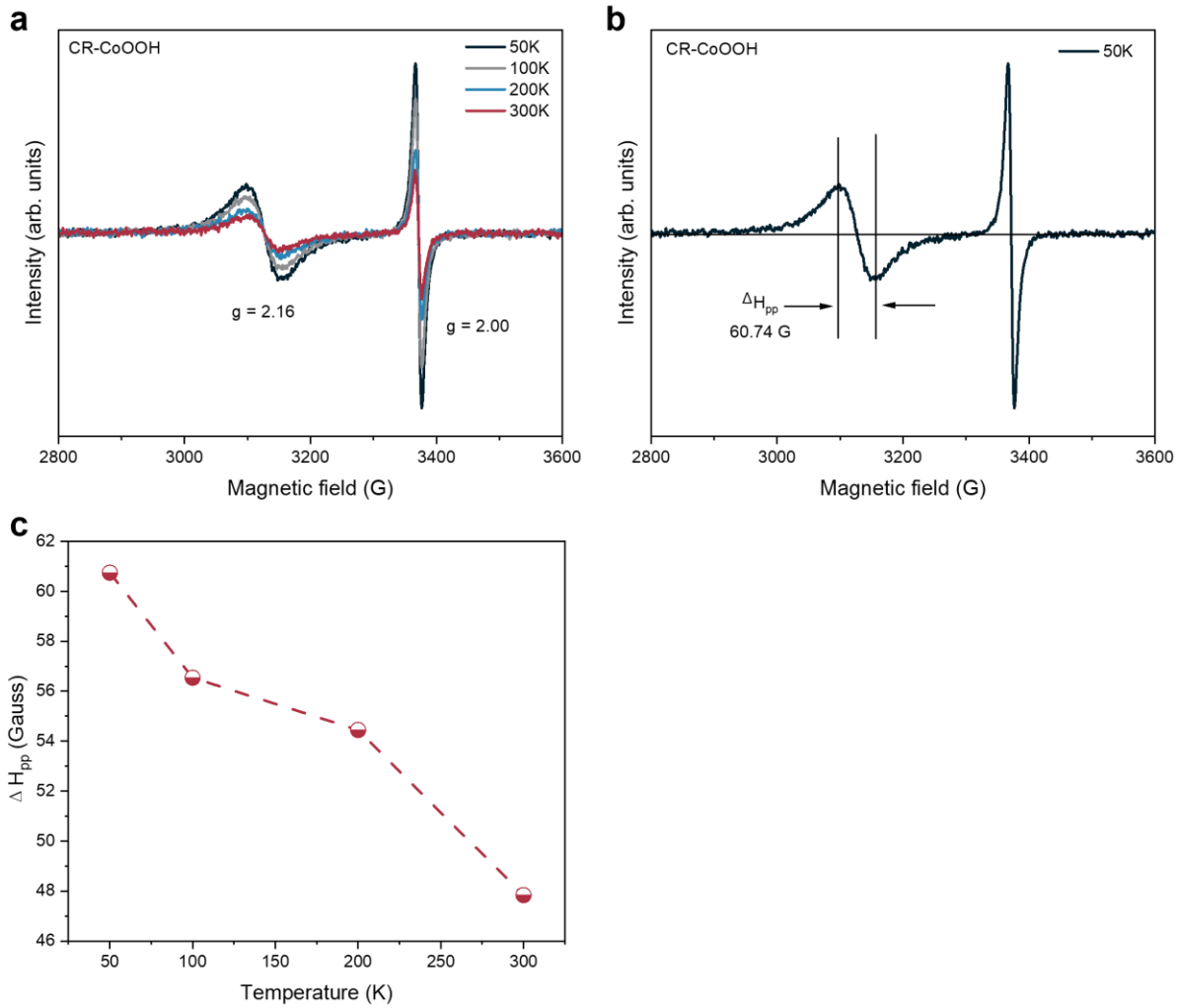


**Supplementary Fig.25 | Temperature-dependent EPR analysis of CR-CoOOH. a**, EPR spectra recorded at 50, 100, 200, and 300 K. **b**, Representative spectrum at 50 K showing the peak-to-peak linewidth ($\Delta H_{pp}$). **c**, Temperature dependence of $\Delta H_{pp}$ extracted from the g ≈ 2.16 resonance.

The temperature-dependent EPR behavior of CR-CoOOH provides further insight into the magnetic interactions among cobalt centers. The monotonic decrease of $\Delta H_{pp}$ with increasing temperature reflects thermally modulated spin-spin interactions, indicative of exchange-coupled localized Co moments. At lower temperatures, the broadened linewidth suggests enhanced exchange correlations and reduced thermal averaging of spin fluctuations.

Such exchange-correlated cobalt spin centers imply a spin-polarizable electronic environment in CR-CoOOH. The presence of exchange interactions can promote partial spin alignment among neighboring Co sites, thereby stabilizing parallel spin configurations in oxygen-derived radical intermediates. This exchange-mediated spin polarization offers a magnetic framework that is consistent with spin-conserved radical oxygen coupling during oxygen evolution.

Rather than arising from long-range ferromagnetic ordering, the observed behavior supports short-range magnetic correlations that modulate the local electronic structure of cobalt and facilitate spin-dependent reaction pathways.

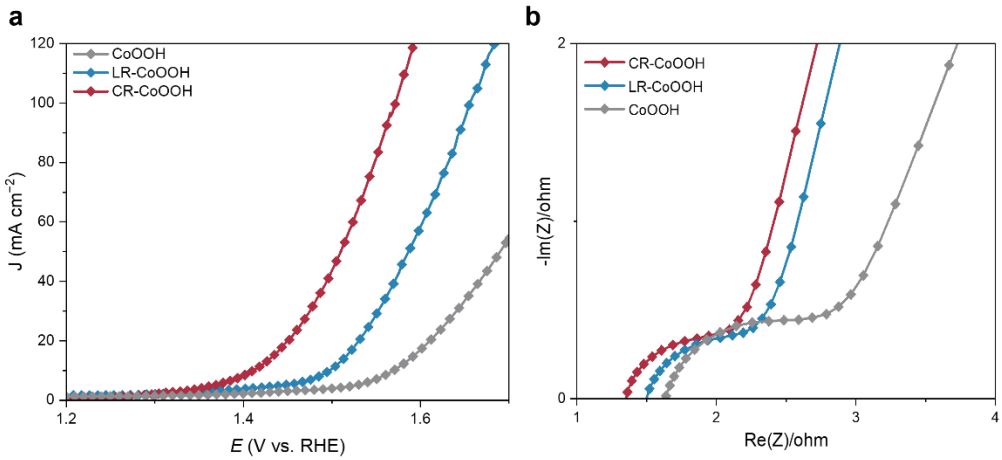


**Supplementary Fig.26 | Electrochemical measurements of CR-CoOOH, LR-CoOOH, and CoOOH. a** Non-*iR*-corrected OER polarization curves. **b** Nyquist plots recorded at open-circuit potential. The resistance (*R*) is determined as 1.33Ω for CR-CoOOH, 1.48Ω for LR-CoOOH, and 1.68Ω for CoOOH. Surface area: 0.5 $cm^{-2}$.

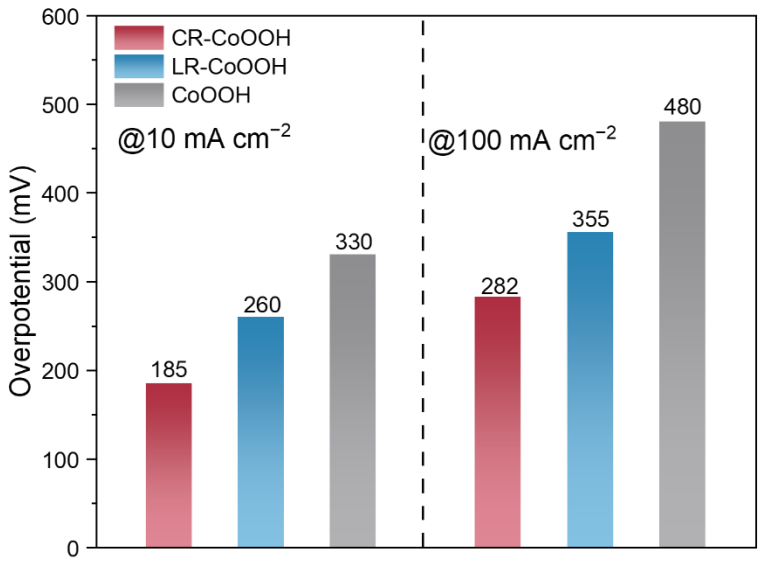


**Supplementary Fig.27 |** Overpotentials required to reach 10 and 100 mA $cm^{-2}$ for CR-CoOOH, LR-CoOOH, and CoOOH.

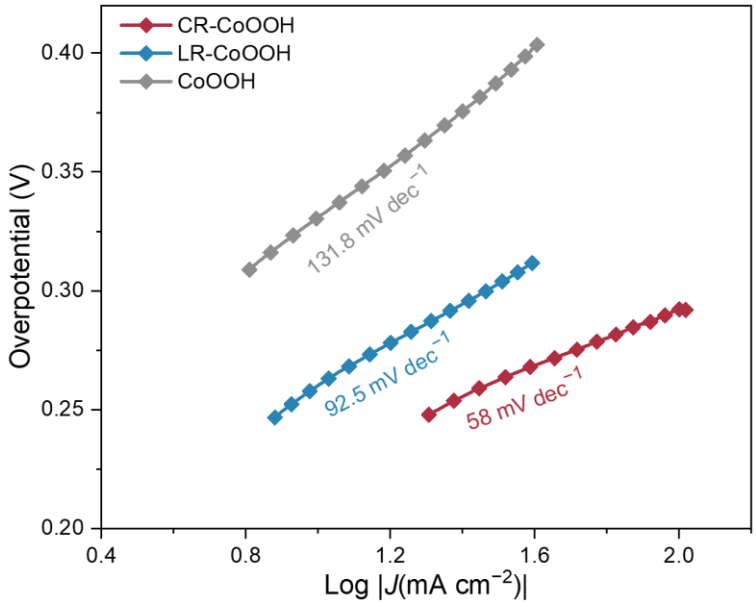


**Supplementary Fig.28 |** Tafel slopes derived from the polarization curves of CR-CoOOH, LR-CoOOH, and CoOOH.

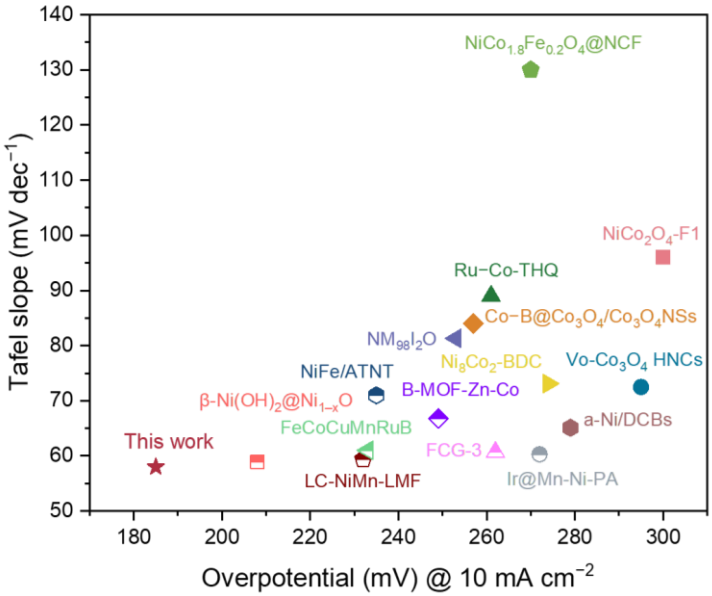


**Supplementary Fig.29 |** Comparison of OER performance with recently reported state-of-the-art OER catalysts. Scatter plot comparing the overpotential at 10 mA cm$^{-2}$ and Tafel slope of CR-CoOOH with representative OER catalysts reported in recent literature from Supplementary Table 3.

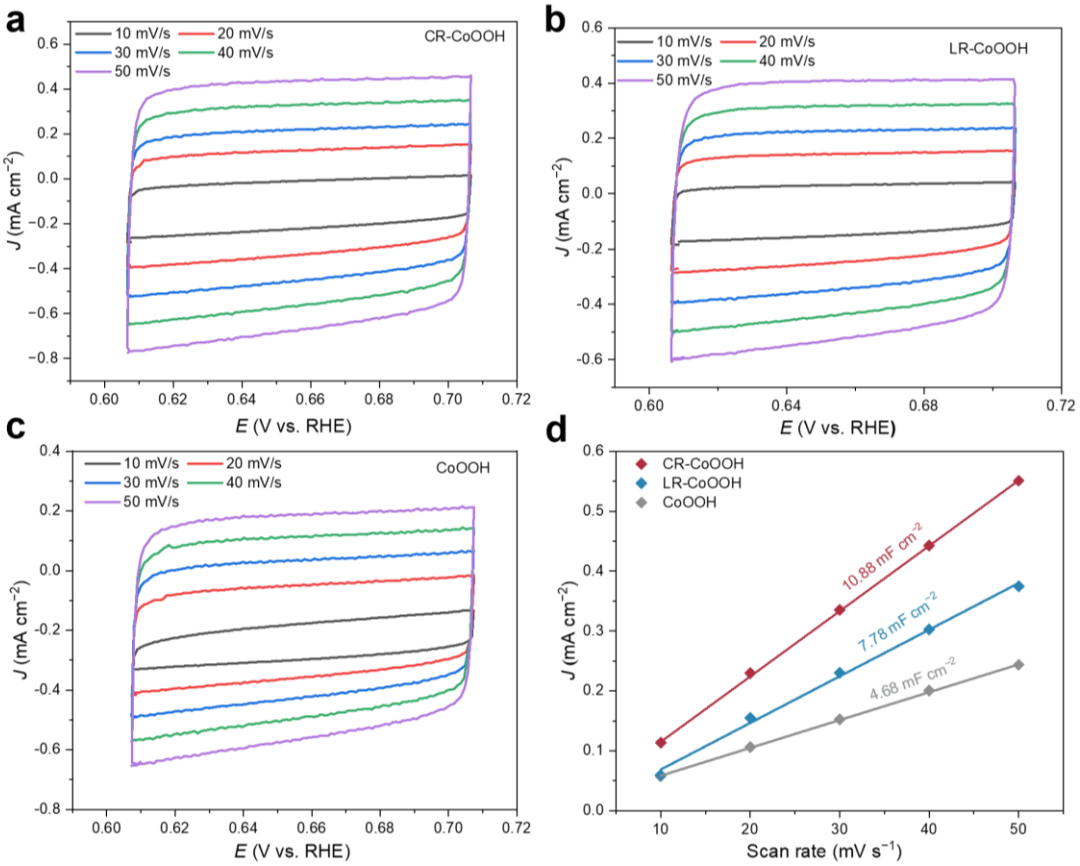


**Supplementary Fig.30 | Determination of electrochemical surface area. a-c** Cyclic voltammograms measured at various scan rates in the non-faradaic potential region for CR-CoOOH, LR-CoOOH, and CoOOH. **d** Linear fitting of the capacitive current density difference ($\Delta J$) as a function of scan rate, from which the double-layer capacitance ($C_{dl}$) is derived.

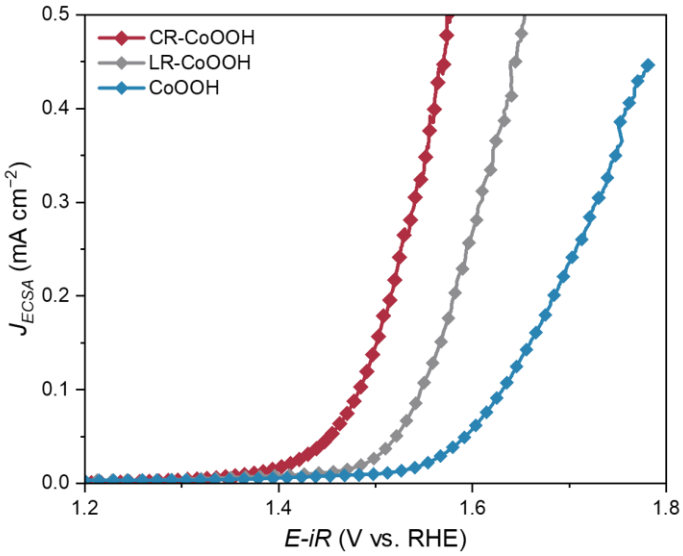


**Supplementary Fig.31 |** Polarization curves of CR-CoOOH, LR-CoOOH, and CoOOH normalized by the electrochemical surface area.

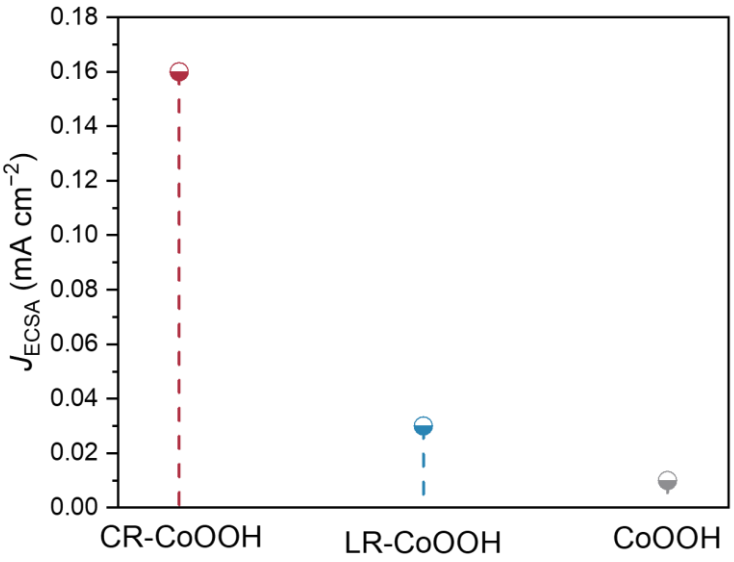


**Supplementary Fig.32 |** Specific current densities of CR-CoOOH, LR-CoOOH, and CoOOH at 1.5 V vs. RHE, normalized by the ECSA.

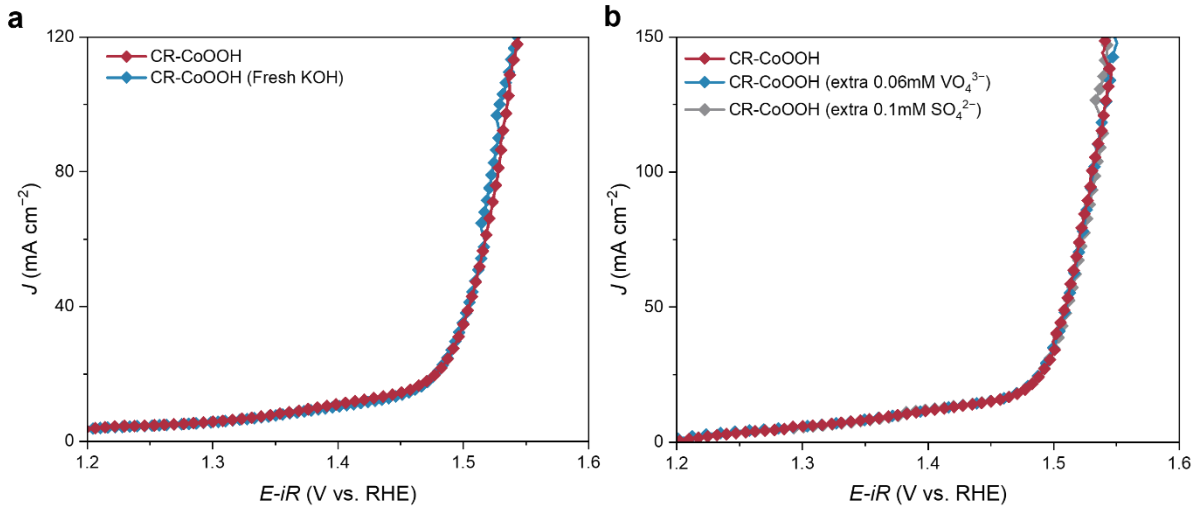


**Supplementary Fig.33 | Control experiments excluding the activity contribution of soluble or weakly adsorbed V/S-derived species. a** OER polarization curves of CR-CoOOH measured before and after transferring the reconstructed electrode into fresh 1 M KOH. **b** OER polarization curves of CR-CoOOH measured in fresh 1 M KOH with and without deliberately added vanadate and sulfate ions.

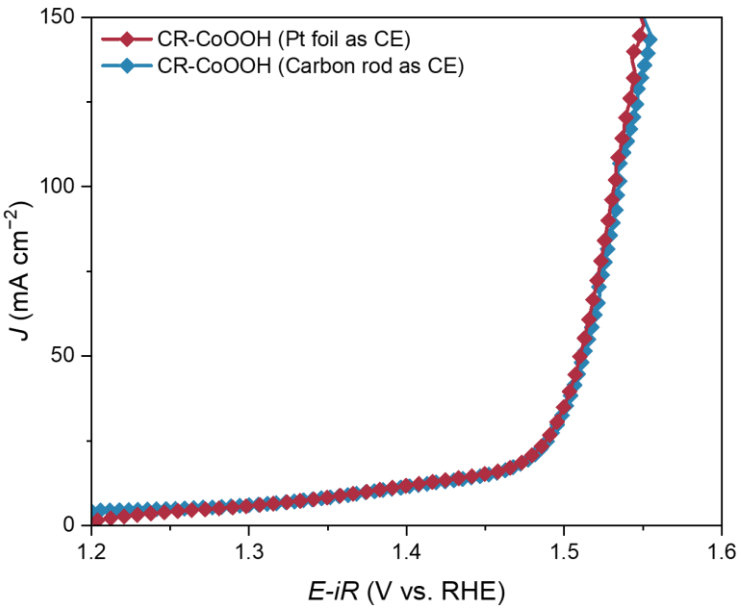


**Supplementary Fig.34 |** OER polarization curves of CR-CoOOH using Pt foil or carbon rod as the counter electrode in 1 M KOH.

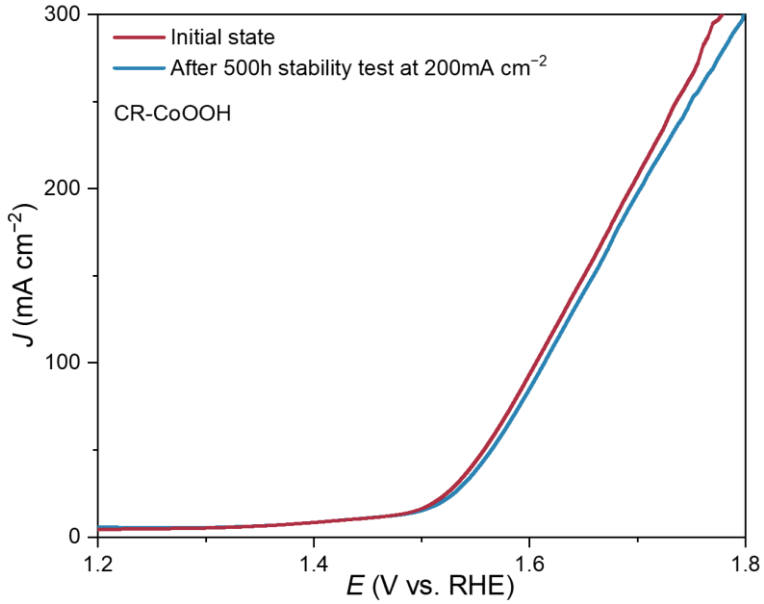


**Supplementary Fig.35 |** LSV curves of CR-CoOOH measured before and after the stability test at 200 mA cm$^{-2}$ for 500 h.

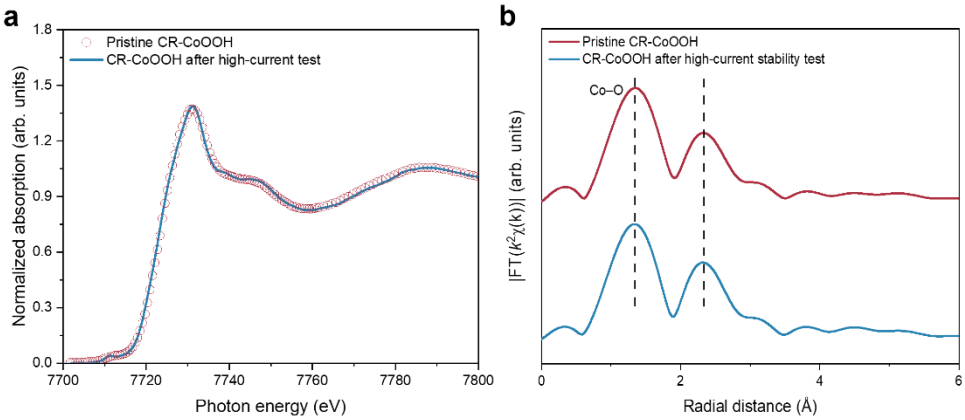


**Supplementary Fig.36 | Structural stability of CR-CoOOH after high-current AEMWE operation**. **a** Co *K*-edge XANES spectra of CR-CoOOH collected before and after 300 h durability testing in an AEM electrolyzer at 2, 4, and 6 A $cm^{-2}$. **b** Fourier-transformed EXAFS spectra showing negligible changes in the local coordination environment.

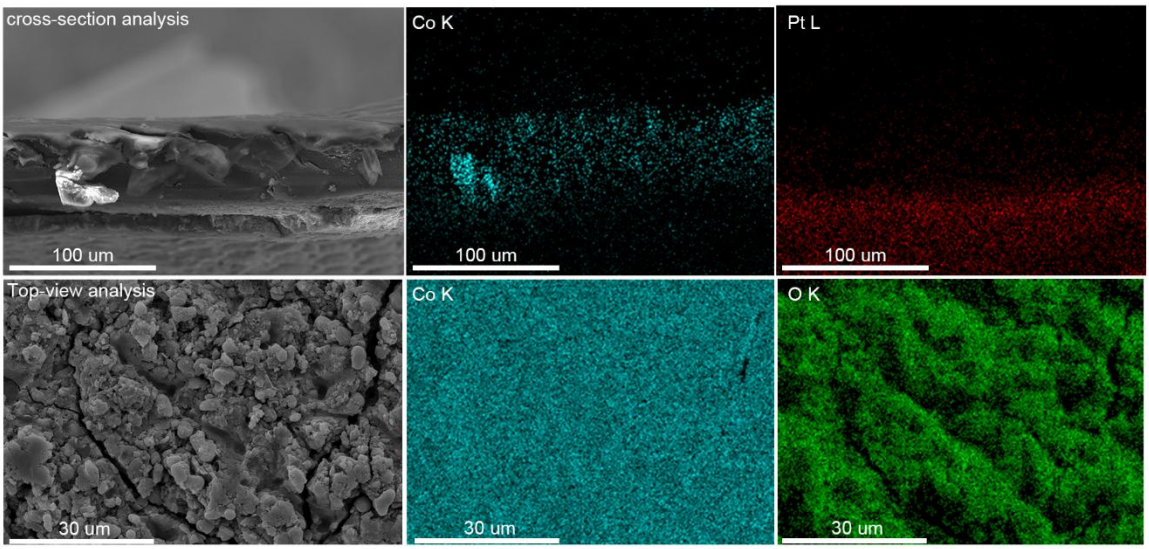


**Supplementary Fig.37 |** SEM/EDS analysis of the MEA after AEMWE stability testing at 1 A $cm^{-2}$ for 100 h.

The catalyst layer/membrane interface remains physically integrated, and the elemental distributions show no obvious Co migration across the membrane or severe catalyst-layer detachment after operation.

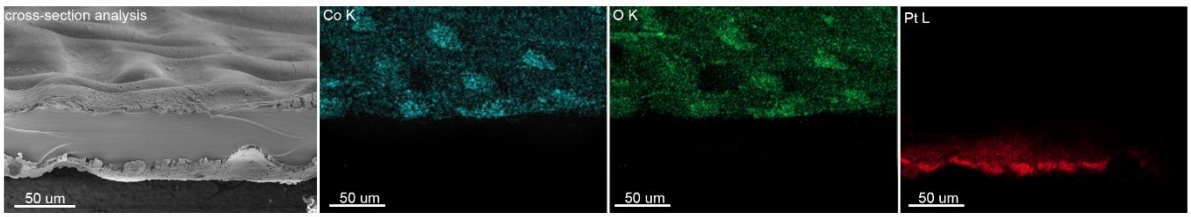


**Supplementary Fig.38 | SEM/EDS analysis of the MEA after AEMWE stability testing at 6 A cm$^{-2}$ for 100 h.** The catalyst layer/membrane interface remains physically integrated, and the elemental distributions show no obvious Co migration across the membrane or severe catalyst-layer detachment after high-current-density operation.

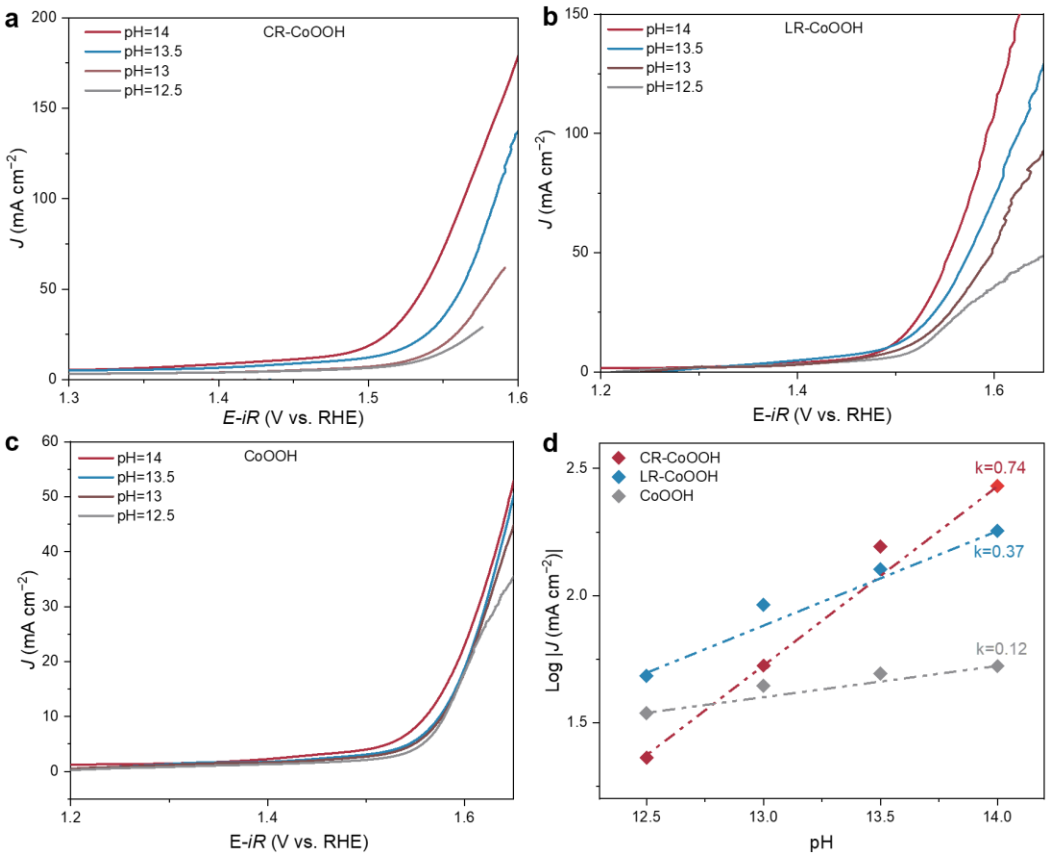


**Supplementary Fig.39 | pH-dependent OER activity of CR-CoOOH, LR-CoOOH, and CoOOH**. **a-c** Linear sweep voltammetry curves measured at different pH conditions. **d** Relationship between catalytic activity and pH with linear fitting to obtain the slope (k).

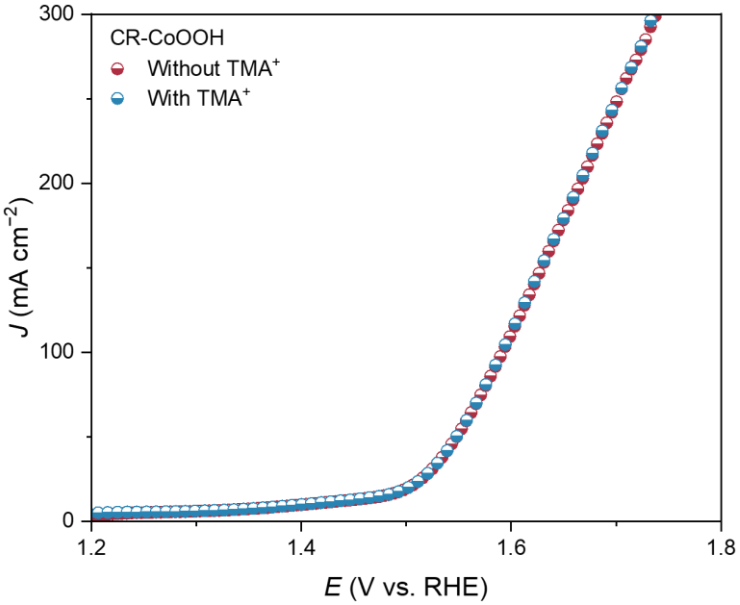


**Supplementary Fig.40 |** LSV curves of CR-CoOOH recorded in alkaline electrolyte with and without tetramethylammonium hydroxide (TMAOH).

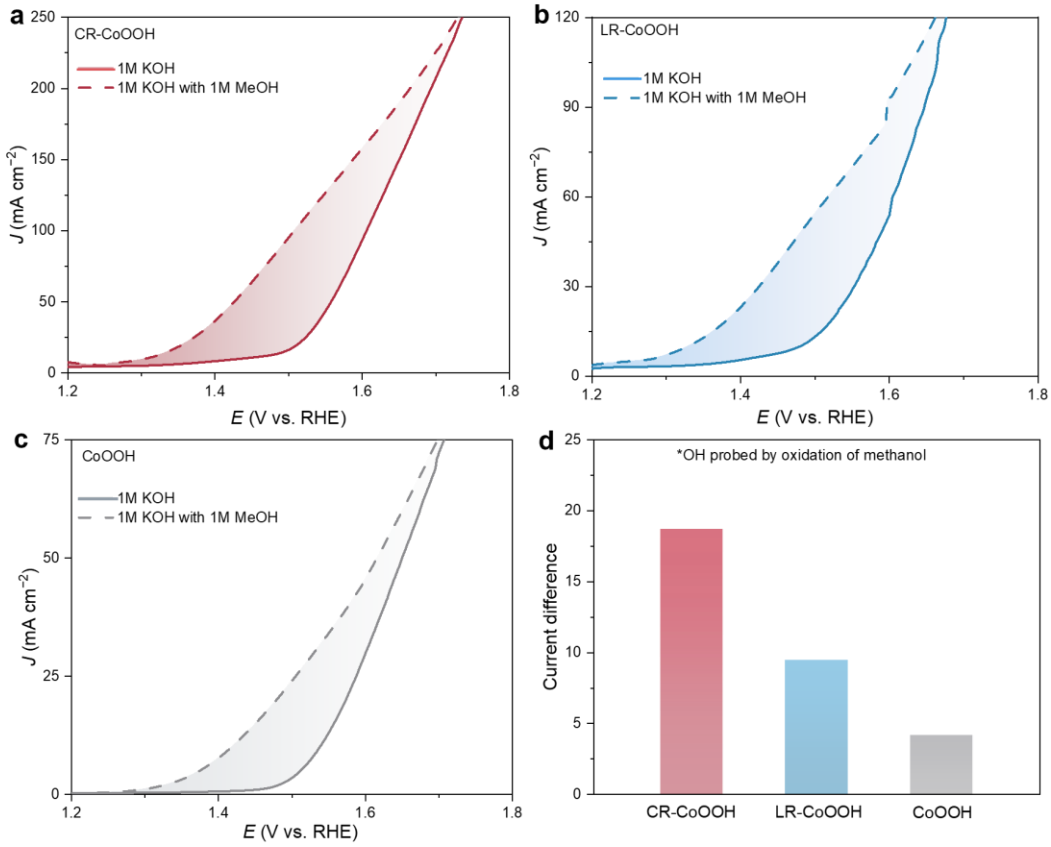


**Supplementary Fig.41 | Probing surface oxygen species using methanol oxidation. a-c** Linear sweep voltammetry curves of CR-CoOOH (a), LR-CoOOH (b), and CoOOH (c) measured in 1 M KOH with and without 1 M methanol. **d** Comparison of current density differences extracted from panels.

Linear sweep voltammetry measurements were performed in 1 M KOH with and without 1 M methanol to probe the reactivity of surface oxygen species. Upon addition of methanol, all samples exhibit an increase in current density, attributable to the oxidation of methanol by surface oxygen intermediates.

Among the three samples, CR-CoOOH shows the most pronounced current enhancement, whereas LR-CoOOH and CoOOH display comparatively smaller responses. The extracted current density differences follow the order CR-CoOOH > LR-CoOOH > CoOOH, indicating a higher density or greater reactivity of surface oxygen species in CR-CoOOH.

Because methanol oxidation is facilitated by reactive oxygen intermediates such as surface $^{*}$OH or oxygen-derived species, the markedly enhanced alcohol-assisted current in CR-CoOOH suggests the presence of more active oxygen species generated during cascade reconstruction. This behavior is consistent with the formation of coordinatively unsaturated Co–O units and a modified electronic environment. Furthermore, the enhanced response supports the existence of spin-polarizable oxygen-hole states in CR-CoOOH, which may participate in radical coupling pathways during oxygen evolution.

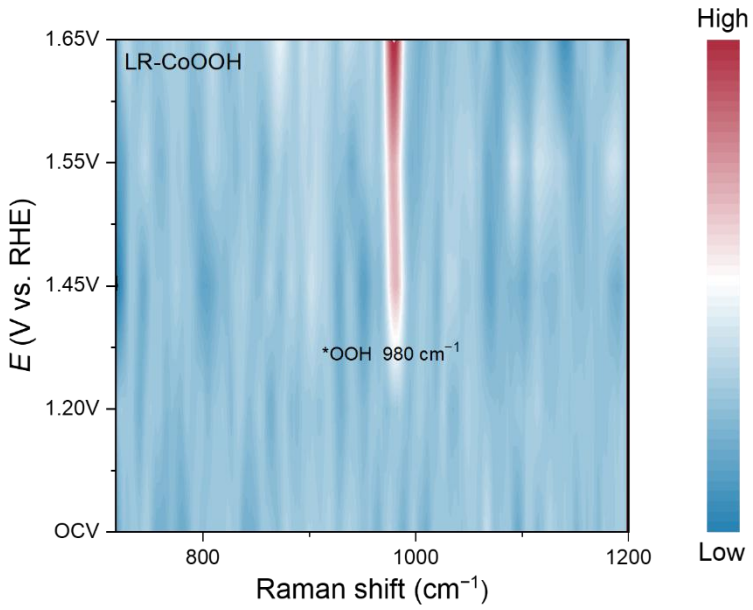


**Supplementary Fig. 42 |** Operando Raman mapping of LR-CoOOH during the OER process. Raman feature centered at ~980 cm$^{-1}$, corresponding to the adsorbed $^{*}$OOH intermediate.

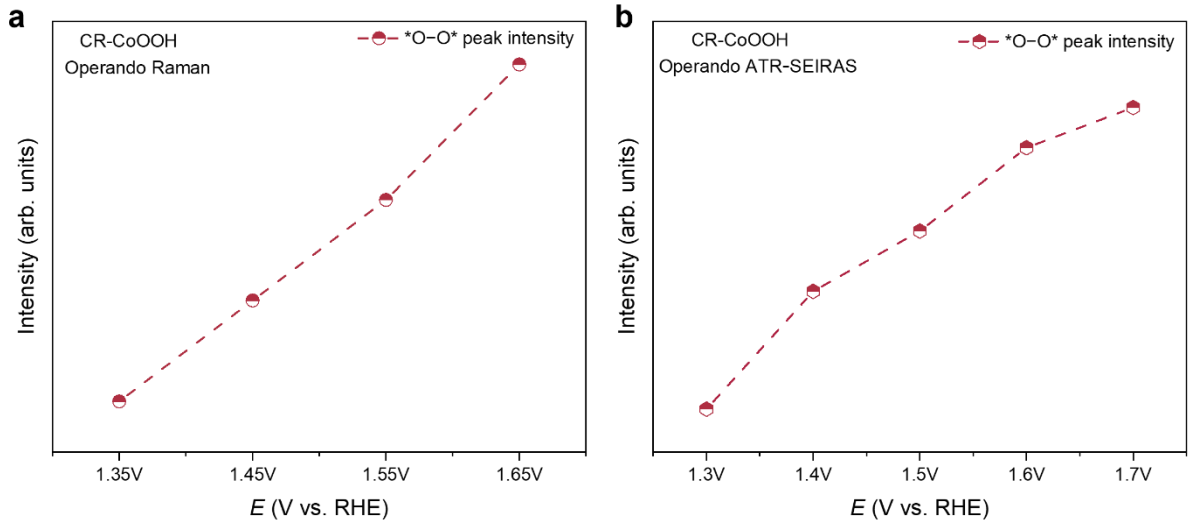


**Supplementary Fig.43 | Potential-dependent evolution of O–O-related vibrational bands under OER conditions. a** Normalized intensities of the O–O-related band derived from operando Raman spectroscopy **b** Normalized intensities of the O–O-related bands derived from operando ATR-SEIRAS. In both measurements, the O–O-related signal increases upon entering the OER-relevant potential region, indicating the potential-driven formation and accumulation of O–O coupling intermediates.

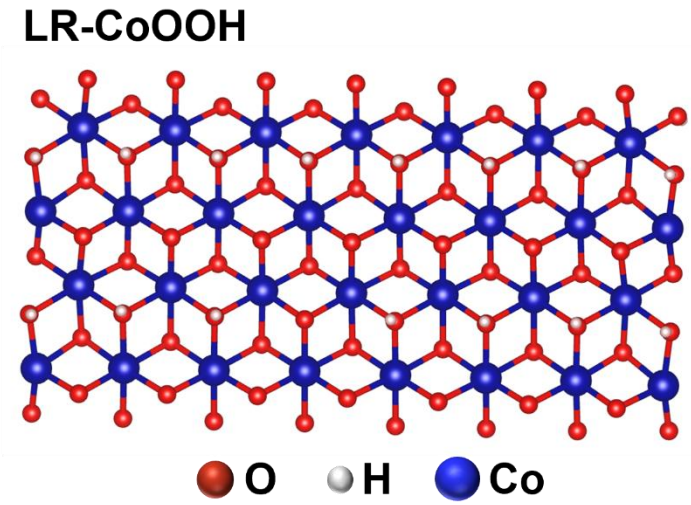


**Supplementary Fig.44 |** Structural model of LR-CoOOH.

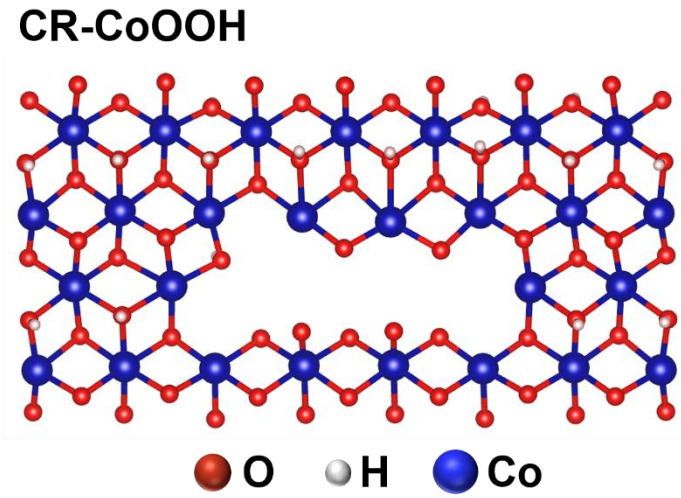


**Supplementary Fig.45 |** Structural model of CR-CoOOH.

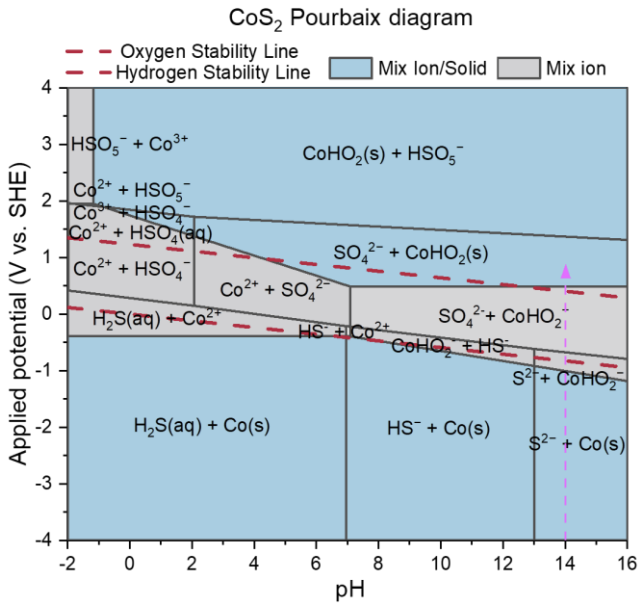


**Supplementary Fig.46 |** Pourbaix-diagram analysis of the thermodynamically stable phase under alkaline OER conditions. Data were generated using the Materials Project (https://next-gen.materialsproject.org/)[1–3].

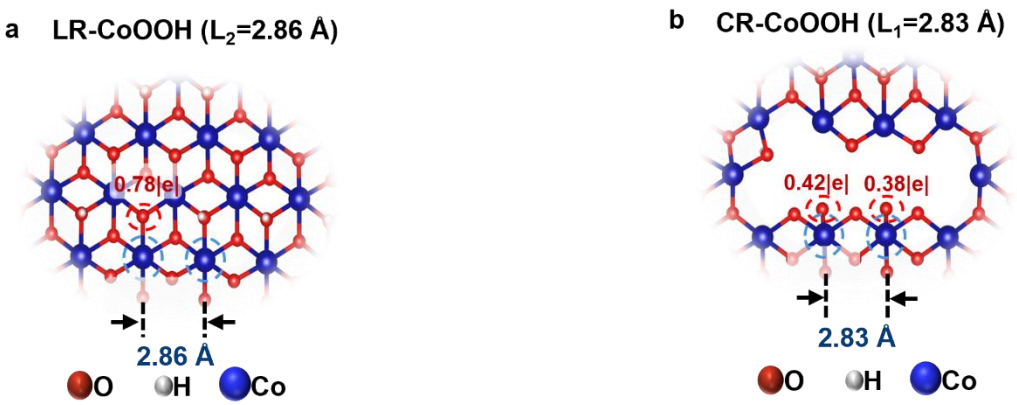


**Supplementary Fig.47 | DFT analysis of Co–Co distance and charge distribution of adsorbed oxygen species**. **a** Structural models of LR-CoOOH. **b** Structural models of CR-CoOOH. The magnified views highlight the adsorption configurations and the corresponding Co–Co distances (2.83 Å for CR-CoOOH and 2.86 Å for LR-CoOOH). The red numbers denote the Bader charge (|e|) of the adsorbed oxygen species ($^*$O), indicating the electron transfer between the catalyst surface and the oxygen intermediate. Blue, red, and white spheres represent Co, O, and H atoms, respectively.

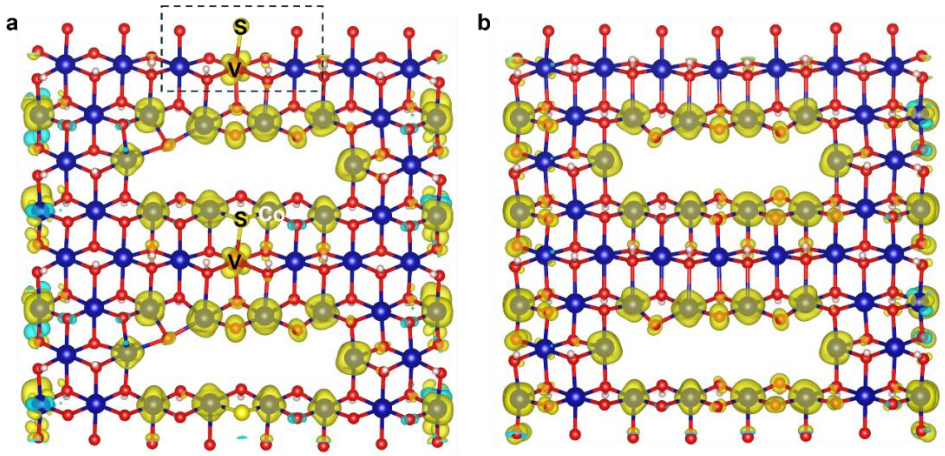


**Supplementary Fig.48 | Spin-density comparison of V/S-containing and V/S-free CR-CoOOH models. a**, Spin-density isosurface of the V/S-containing CR-CoOOH model. **b** Spin-density isosurface of the V/S-free CR-CoOOH model.

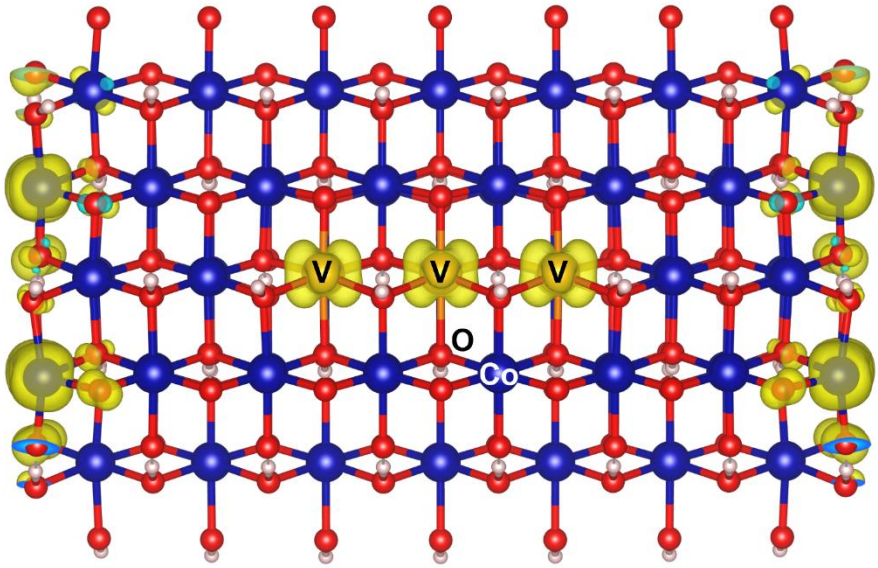


**Supplementary Fig.49 |** Spin-density isosurface of V–CoOOH.

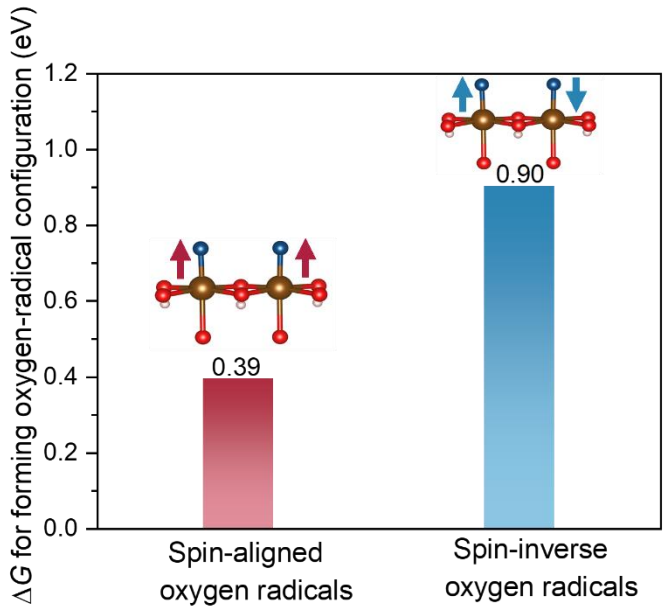


**Supplementary Fig.50** | Energetic comparison of spin-aligned and spin-inverse oxygen-radical configurations.

Calculated formation energies of spin-aligned and spin-inverse oxygen-radical configurations involved in the $O_2$ formation process on CR-CoOOH.

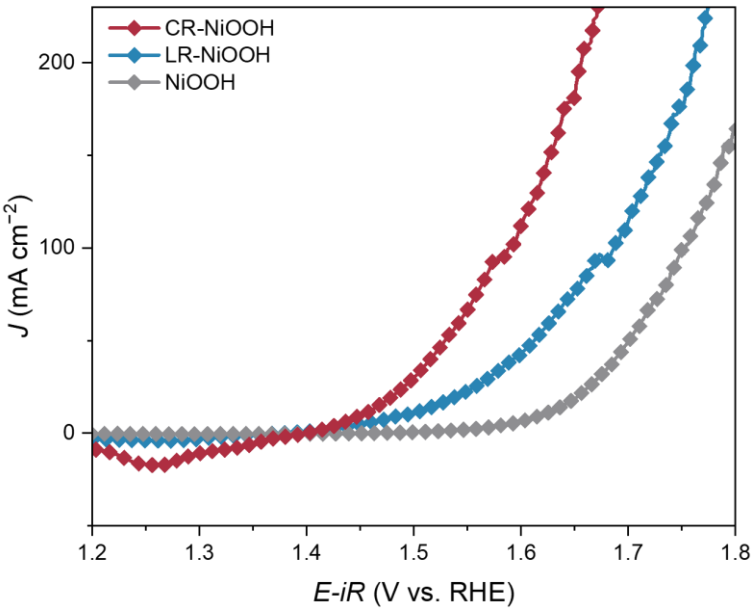


**Supplementary Fig.51 |** LSV curves of CR-NiOOH, LR-NiOOH, and NiOOH in fresh 1 M KOH.

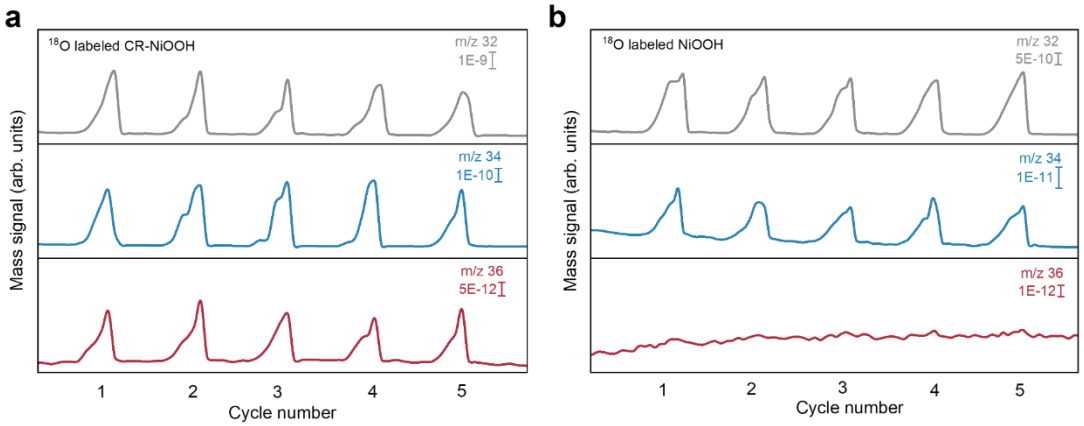


**Supplementary Fig.52 | Operando DEMS characterization of NiOOH-based catalysts. a** Operando DEMS signals of $O_2$ products for $^{18}$O-labeled CR-NiOOH. **b** Operando DEMS signals of $O_2$ products for $^{18}$O-labeled NiOOH.

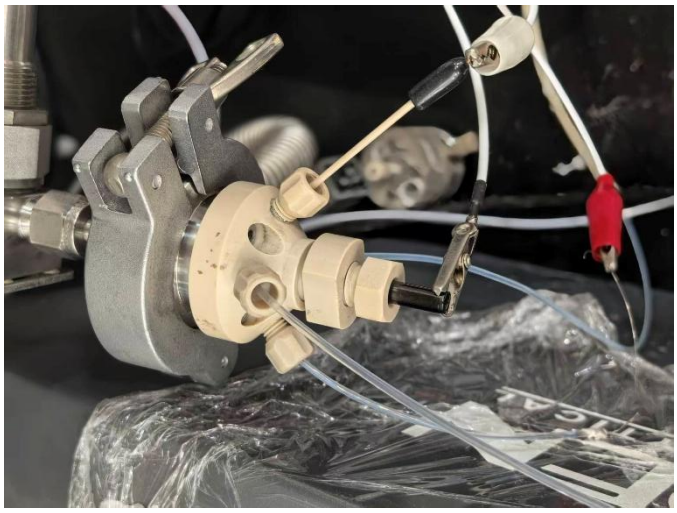

**Supplementary Fig.53 |** Schematic of DEMS electrochemical cell.

The L-DP01 membrane from Shanghai Linglu is employed. Electrochemical testing was conducted in a three-electrode configuration with a carbon-cloth-supported catalyst as the working electrode, a Pt wire as the counter electrode, and a Hg/HgO electrode as the reference electrode. The electrolyte is 1 M KOH.

**Supplementary Table 1 | ICP analysis of V–$CoS_2$ after activation for different durations**

| V-$CoS_2$ Stage | Mass ratio of Co (wt%) | Mass ratio of S (wt%) | Mass ratio of V (wt%) |
|---|---|---|---|
| 0 h | 37.92 | 27.63 | 3.02 |
| 2 h | 20.28 | 0.28 | 0.25 |
| 4 h | 20.03 | 0.23 | 0.19 |
| 6h | 19.96 | 0.06 | 0.03 |
| 10 h | 21.55 | N/A | N/A |

Elemental contents were determined by ICP analysis after acid digestion of the corresponding samples.

**Supplementary Table 2 |** FT-EXAFS fitting results of R-CoOOH and S-CoOOH, where CN is the coordination number, $\sigma^2$ is the Debye-Waller factor, $\Delta E_0$ is the shift in absorption edge energy, R is the bond length, and R-factor means Residual factor.

| Sample | Path | CN | $\sigma^2$ | $\Delta E_0$ | $R$ | R-factor |
|---|---|---|---|---|---|---|
| CoOOH | Co—O | 6.05±0.40 | 0.0015± 0.0009 | 2.772±0.619 | 1.900±0.0053 | 0.002 |
| LR-CoOOH | Co—O | 5.44±0.45 | 0.0045± 0.0013 | 0.436±0.495 | 1.912±0.0053 | 0.004 |
| CR-CoOOH | Co—O | 4.22±0.56 | 0.006± 0.0012 | -1.411±1.429 | 1.907±0.007 | 0.008 |

**Supplementary Table 3 |** Comparison of the overpotential and Tafel slope of CR-CoOOH with reported OER catalysts.

| Catalysts | $\eta$ (mV) at 10 mA $cm^{-2}$ | Tafel slope (mV $dec^{-1}$) | Durability (h) | Loading mass (mg $cm^{-2}$) | Electrolyte resistance (Ω) | Ref. |
|---|---|---|---|---|---|---|
| CR-CoOOH | 185 | 58 | 500 (200mA $cm^{-2}$) | 0.75 | 1.4 | This work |
| FCG-3 | 262 | 60.7 | 30 (10mA $cm^{-2}$) | 1 | 4.41 | ref[4] |
| Ir@Mn-Ni-PA | 272 | 60.3 | 100 (10mA $cm^{-2}$) | N/A | 1.51 | ref[5] |
| $NM_{98}I_2O$ | 253 | 81.3 | 1000 (10mA $cm^{-2}$) | 0.25 | 2.6 | ref[6] |
| a-Ni/DCBs | 279 | 65.1 | 200 (10mA $cm^{-2}$) | N/A | N/A | ref[7] |
| Ru−Co-THQ | 261 | 89 | 120 (250mA $cm^{-2}$) | 0.42 | 7.56 | ref[8] |
| NiFe/ATNT | 235 | 71 | 100 (10mA $cm^{-2}$) | 5 | 1.9 | ref[9] |
| LC-NiMn-LMF | 232 | 59.4 | 100 (500mA $cm^{-2}$) | N/A | 1.8 | ref[10] |
| $NiCo_2O_4$-F1 | 300 | 96 | 100 (100mA $cm^{-2}$) | 3 | 9.774 | ref[11] |
| $NiCo_{1.8}Fe_{0.2}O_4$@NCF | 270 | 130 | 20 (100mA $cm^{-2}$) | 0.5 | N/A | ref[12] |
| $V_o$-$Co_3O_4$ HNCs | 295 | 72.5 | 130 (20mA $cm^{-2}$) | 1 | N/A | ref[13] |
| Co−B@$Co_3O_4$/$Co_3O_4$NSs | 257 | 84 | 16 (20mA $cm^{-2}$) | 0.254 | 12 | ref[14] |
| B-MOF-Zn-Co | 249 | 66.8 | 300 (100mA $cm^{-2}$) | N/A | 1.5 | ref[15] |
| FeCoCuMnRuB | 233 | 61 | 200 (10mA $cm^{-2}$) | N/A | 7.097 | ref[16] |
| $Ni_8Co_2$-BDC | 274 | 73.1 | 48 (10mA $cm^{-2}$) | 1 | N/A | ref[17] |
| β-$Ni(OH)_2$@$Ni_{1-x}O$ | 208 | 58.9 | 40 (10mA $cm^{-2}$) | N/A | N/A | ref[18] |

**Supplementary Table 4 |** Performance of AEMWE assembled with recently reported anodic catalysts.

| Anode | Cell voltage (V@1A $cm^{-2}$) | Current density @ 2 V (A $cm^{-2}$) | Stability (h) | Degradation rate (mV $h^{-1}$) | AEM loading (mg $cm^{-2}$) | Reference |
|---|---|---|---|---|---|---|
| CR-CoOOH | 1.64 | 6.3 | 2000 | 0.05 | 1 | This work |
| W-$Co_3O_4$ | 2.12 | 1.8 | 100 | 0.1 | 3 | ref[19] |
| N-CoO | 1.7 | 2 | 300 | 0.1 | 3 | ref[20] |
| CoOOH-*l* | 1.69 | 3.4 | 1200 | 0.09 | 5 | ref[21] |
| Fe@Co oxide | 1.72 | 3.05 | 1000 | 0.2 | 2 | ref[22] |
| $Ni_3Fe$ LDH | 1.74 | 2.07 | 400 | 0.093 | 2 | ref[23] |
| NiFe LDH | 1.91 | 1.3 | 100 | 0.09 | 1 | ref[24] |
| Ru-$Co_2Ni$@NCNT | 1.87 | 1.5 | 500 | 0.1 | 1.2 | ref[25] |
| FeNiPt@C | 1.95 | 1.02 | 90 | 1.11 | 2 | ref[26] |
| $FCM_{0.47}$ | 1.76 | 2.2 | 500 | 0.46 | 2 | ref[27] |
| NiFe/Ni-S | 1.8 | 1.2 | 400 | 0.37 | 1 | ref[28] |
| $Ni_{0.8}Fe_{0.2}Mn_{0.1}Se_2$ | 1.68 | 1.5 | 300 | 0.59 | 1 | ref[29] |
| $NiFe_2O_4$-50 | 1.68 | 2.9 | 1000 | 0.24 | 1.5 | ref[30] |

**References:**


1. Singh, A. K. *et al.* Electrochemical Stability of Metastable Materials. *Chem. Mater.* **29**, 10159–10167 (2017).
2. Jain, A. *et al.* Commentary: The Materials Project: A materials genome approach to accelerating materials innovation. *APL Mater.* **1**, 011002 (2013).
3. Patel, A. M., Nørskov, J. K., Persson, K. A. & Montoya, J. H. Efficient Pourbaix diagrams of many-element compounds. *Phys. Chem. Chem. Phys.* **21**, 25323–25327 (2019).
4. Pandit, A., De, A., Palakkal, A. S., Kundu, S. & Neogi, S. Antagonistically Functionalized Cobalt-Organic Framework Enabling Bifunctional Water Splitting and One-Pot Synthesis of Bioactive 4H-Pyrans via Synergistic Catalysis. *Small* **22**, e14442 (2026).
5. Ngo, Q. P. *et al.* Tailored Design of Iridium Single Atoms on Mn–Ni-Phytate with Robust Bifunctionality for Enhanced Anion Exchange Membrane Water Electrolysis. *Adv. Energy Mater.* **16**, e06645 (2026).
6. Zhu, J. *et al.* Selective Atomic Incorporation: Synergistically Tailoring Adsorbate Evolution and Lattice Oxygen Pathways for Enhanced Water Oxidation. *Angew. Chem. Int. Ed.* **64**, e202516903 (2025).
7. Zhu, J., Zhao, J.-W., Luan, D. & Lou, X. W. (David). Oxygen-Coordinated Single-Atom Nickel Catalysts Derived from Water-Induced Metal–Organic Framework Aerogel for Efficient Water Oxidation. *Angew. Chem. Int. Ed.* **64**, e202500261 (2025).
8. Wang, Y. *et al.* Metal–Oxygen Bonding-Induced Structural Transition Regulation in Co-THQ for High-Performance OER. *ACS Catal.* **15**, 17040–17053 (2025).
9. Shaik, S. *et al.* Rapid Outgassing of Hydrophilic TiO2 Electrodes Achieves Long-Term Stability of Anion Exchange Membrane Water Electrolyzers. *Nano-Micro Lett.* **17**, 186 (2025).
10. Huang, Q. *et al.* Converting the Negative Ni-Mn Synergy into Positive in Lower-Coordination Layered Double Hydroxide/Metal-Organic Framework Heterojunction for Efficient Water and Urea Electrooxidation. *Adv. Funct. Mater.* **35**, 2506007 (2025).
11. Yue, Y. *et al.* Fluorine Engineering Induces Phase Transformation in NiCo2O4 for Enhanced Active Motifs Formation in Oxygen Evolution Reaction. *Adv. Mater.* **37**, 2418058 (2025).
12. Liu, Y. *et al.* Fe, N-Inducing Interfacial Electron Redistribution in NiCo Spinel on Biomass-Derived Carbon for Bi-functional Oxygen Conversion. *Angew. Chem.* **136**, e202319983 (2024).
13. Rong, C. *et al.* Defect-balanced active and stable Co3O4−x for proton exchange membrane water electrolysis at ampere-level current density. *Energy Environ. Sci.* **17**, 4196–4204 (2024).
14. Zhong, X. *et al.* Spatially and Temporally Resolved Dynamic Response of Co-Based Composite Interface during the Oxygen Evolution Reaction. *J. Am. Chem. Soc.* **146**, 7467–7479 (2024).
15. Lin, X. *et al.* In Situ Electrochemical Restructuring B-Doped Metal–Organic Frameworks as Efficient OER Electrocatalysts for Stable Anion Exchange Membrane Water Electrolysis. *Small* **20**, 2308517 (2024).
16. Liu, L. *et al.* FeCoCuMnRuB Nanobox with Dual Driving of High-Entropy and Electron-Trap Effects as the Efficient Electrocatalyst for Water Oxidation. *Nano Lett.* **24**, 2831–2838 (2024).
17. Zhou, J. *et al.* Amorphization Engineering of Bimetallic Metal-Organic Frameworks to Identify Volcano-Type Trend toward Oxygen Evolution Reaction. *Adv. Funct. Mater.* **34**, 2304380 (2024).
18. Yao, Y. *et al.* Facet-Dependent Surface Restructuring on Nickel (Oxy)hydroxides: A Self-Activation Process for Enhanced Oxygen Evolution Reaction. *J. Am. Chem. Soc.* **146**, 15219–15229 (2024).
19. Wang, Y. *et al.* High-Density W Single Atoms in Two-Dimensional Spinel Oxide Break the Structural Integrity for Enhanced Oxygen Evolution Catalysis. *J. Am. Chem. Soc.* **147**, 32249–32262 (2025).

20. Yu, P.-C. *et al.* Nitrogen-Mediated Promotion of Cobalt-Based Oxygen Evolution Catalyst for Practical Anion-Exchange Membrane Electrolysis. *J. Am. Chem. Soc.* **146**, 20379–20390 (2024).
21. Zhao, J. *et al.* Localizing the Long-Range Disorder of Reconstructed Cobalt Oxyhydroxides for Anion Exchange Membrane Water Electrolysis. *Angew. Chem.* **137**, e202513592 (2025).
22. Han, S., Park, J. & Yoon, J. Surface Reconstruction of Co-based Catalysts for Enhanced Oxygen Evolution Activity in Anion Exchange Membrane Water Electrolysis. *Adv. Funct. Mater.* **34**, 2314573 (2024).
23. Jiang, W. *et al.* Composition-Dependent Morphology, Structure, and Catalytical Performance of Nickel–Iron Layered Double Hydroxide as Highly-Efficient and Stable Anode Catalyst in Anion Exchange Membrane Water Electrolysis. *Adv. Funct. Mater.* **32**, 2203520 (2022).
24. Zeng, L. *et al.* Single-Atom Cr–N4 Sites with High Oxophilicity Interfaced with Pt Atomic Clusters for Practical Alkaline Hydrogen Evolution Catalysis. *J. Am. Chem. Soc.* **145**, 21432–21441 (2023).
25. Majumdar, A. *et al.* Strain Engineering of Ru–Co2Ni Nanoalloy Encapsulated with Carbon Nanotubes for Efficient Anion and Proton Exchange Membrane Water Electrolysis. *Adv. Funct. Mater.* **35**, 2420517 (2025).
26. Pan, Y. *et al.* Constructing FeNiPt@C Trifunctional Catalyst by High Spin-Induced Water Oxidation Activity for Zn-Air Battery and Anion Exchange Membrane Water Electrolyzer. *Adv. Sci.* **11**, 2308205 (2024).
27. Woo, J., Han, S. & Yoon, J. Mn-doped Sequentially Electrodeposited Co-based Oxygen Evolution Catalyst for Efficient Anion Exchange Membrane Water Electrolysis. *ACS Appl. Mater. Interfaces* **16**, 23288–23295 (2024).
28. Chen, B. *et al.* Interface-Engineered NiFe/Ni-S Nanoparticles for Reliable Alkaline Oxygen Production at Industrial Current: A Sulfur Source Confinement Strategy. *Small* **20**, 2310737 (2024).
29. Wang, S., Li, M., Tang, H. & Zhang, H. Interstitial Manganese-Tuned Nickel–Iron Diselenide Anode for Efficient and Durable Anion Exchange Membrane Water Electrolysis. *Small* **21**, 2411397 (2025).
30. Wang, X. *et al.* Ni/Fe based electrocatalyst for highly-efficient anion exchange membrane water electrolysis. *J. Power Sources* **591**, 233819 (2024).